Louisiana State University
LSU Digital Commons

LSU Master's Theses | Graduate School

May 2022

A New Insight into Fungal Cell Wall Architecture by Functional Genomics and Solid-State NMR along with Recent Advancements in Dynamic Nuclear Polarization for Analyzing Biomolecules

Arnab Chakraborty

Follow this and additional works at: https://digitalcommons.lsu.edu/gradschool_theses

 Part of the Analytical Chemistry Commons, Biochemistry Commons, Physical Chemistry Commons, and the Structural Biology Commons

Recommended Citation

Chakraborty, Arnab, "A New Insight into Fungal Cell Wall Architecture by Functional Genomics and Solid-State NMR along with Recent Advancements in Dynamic Nuclear Polarization for Analyzing Biomolecules" (2022). *LSU Master's Theses*. 5589.
https://digitalcommons.lsu.edu/gradschool_theses/5589

This Thesis is brought to you for free and open access by the Graduate School at LSU Digital Commons. It has been accepted for inclusion in LSU Master's Theses by an authorized graduate school editor of LSU Digital Commons. For more information, please contact gradetd@lsu.edu.

A New Insight Into Fungal Cell Wall Architecture By Functional Genomics And Solid-State NMR Along With Recent Advancements In Dynamic Nuclear Polarization For Analyzing Biomolecules

A Thesis

Submitted to the Graduate Faculty of the
Louisiana State University and
Agricultural and Mechanical College
in partial fulfillment of the
requirements for the degree of
Master of Science

in

The Department of Chemistry

by
Arnab Chakraborty
B.Sc. University of Dhaka .2017
August 2022

Table of Contents

Abstract iii

Chapter 1. Introduction 1

Chapter 2. A Molecular Vision of Fungal Cell Wall Organization by Functional Genomics and Solid-State NMR 6

Chapter 3. Biomolecular Complex Viewed by Dynamic Nuclear Polarization Solid-State NMR Spectroscopy 25

Chapter 4. Conclusion 36

Appendix A. Supplementary Information of Chapter 2 38

Appendix B. Permission for reuse 65

References: 68

Vita 80

Abstract

This dissertation summarizes the findings related to the way by which supramolecular architecture of fungal cell wall changes with genetic mutation, dispensing genes responsible for biosynthesis of cell wall polysaccharides. This is necessary because without perfect picture of how supramolecular assembly changes with genetic mutation it is hard to assess new anti-fungal targets. Alongside this we have highlighted how recent advancement into Dynamic Nuclear Polarization (DNP) methods improved characterization of biomolecules both in case of labeled and unlabeled samples.

First study utilized Solid-state NMR (SSNMR) which is a non-destructive technique hence enabled us for the first time to deduce how nanoscale packing, hydration, and mobility of inner cell wall polysaccharides: α-1,3-glucan, β-glucan and chitin changes when either α-1,3-glucan or chitin is removed. Although galactomannan (GM) and galactosaminogalactan (GAG) lies in the exterior still GM deficiency brought about changes in the inner cell wall which is mysterious. GAG has an important role is masking β-1,3-glucan from recognition by human immune system hence its identification using SSNMR was very crucial. At the same time, we were surprised how polysaccharide deficiency brought about drastic changes in the protein region. Apart from this we have also treated the control strain with hot alkali and demonstrated that α-1,3-glucan cannot be removed completely which indicates its involvement in forming fibrils in the inner cell wall with β-glucan and chitin. The biggest surprise came in when repeated alkaline treatment could not remove valine. This is a clear indication that valine is involved in forming glycoprotein linkages. This model which depicts architectural change will improve our understanding of the way fungi responds to environmental stress.

The recent advancements in magic angle spin dynamic nuclear polarization (MAS-DNP) enabled atomic-level characterization of biomolecules. Main factor contributing to this success has been preparation of DNP juice compatible with several biomolecules and hence allowing huge sensitivity enhancements. There are several interactions which were brought to light by MAS-DNP. For example, interactions between carbohydrates, proteins, and ligands. Hence in the future we can expect to see more utilization of MAS-DNP on biological research which will induce rapid development in its instrumentation.

Chapter 1. Introduction

Background and significance

Fungi are extremely abundant, and they have well developed cellular organs such as the membrane-enclosed nucleus. They have caused superficial infections to billions of people. The examples of fungal infections are athlete's foot, mucosal infections, etc. Although these may sound trivial matters, fungi have the potential to cause life-threatening infections [1]. These invasive infections occur to more than two million individuals worldwide, with a fluctuating mortality rate ranging from 20% to 95% [2]. *A. fumigatus* affects more than 200,000 patients worldwide with a mortality rate of 50% for patients with treatment and close to 100% for those without treatment. Nearly 25% of all leukemia patients experienced aspergillosis with an exceptionally high mortality rate of around 90% [2-4]. Heretofore multiple pathogens such as *Aspergillus fumigatus, Candida albicans,* and *Cryptococcus neoformans* are considered supervillain with the ability to cause fatal infections in immunocompromised patients [5-8]. More importantly, they can exist in various forms owing to genetic mutations [9-13].

Most antifungal agents are either ineffective or toxic. The existing compounds target the ergosterols in fungal cell membrane but they also bind to cholesterols in human membranes[14, 15]. Another compound, Amphotericin B, failed to prevent death in more than half of the patients with invasive aspergillosis, proving its lack of efficacy [16]. Fortunately, cell wall-targeted antifungal agents have been developed and they exhibit reduced toxicity. These antifungal drugs disrupt glucan synthesis as well as cell wall integrity [17-19]. Most of the carbohydrates present in the fungal cell wall are absent in human cells [20, 21]. Fungal cells are covered by these cell walls, which is a dynamic structure with a rigid exoskeleton, when exposed to external environments that are not conducive to fungi vegetation, the cell wall structure undergoes compositional changes via genetic

mutations. The unsuitable environment can be a direct consequence of climate change or drug treatment. The goal of drug researchers is to develop drugs that will not allow the fungi to adapt even through composition changes. This makes cell wall studies crucial to serve their purpose.

The fungal cell wall contains mainly glucans and glycoproteins. It contains 50-60% glucans, 20-30% glycoproteins, and a small portion of chitin, for example, 10-20% [20]. The cell wall architecture is unclear. Most fungi consist of covalent linkages between β-1,3-glucan, α-1,3-glucan, chitin, and galactomannan [22-24] making the inner rigid core hydrophobic and impenetrable by air or moisture whereas the mobile portion consists of galactomannan and galactosaminogalactan. The cell wall strength is further increased by the accumulation of β-1,4-glucan and β-1,6-glucan in some fungi [25, 26] . This enables the microfibrils to withstand high turgor pressure of around 0.25-0.5 Mpa [27]. These conclusions have been reached by enzymatic hydrolysis and gel permeation chromatography [28], which requires destruction of the cell wall indeed set up a huge barrier in developing an appropriate structure capable of solving the conundrum. Hence it is crucial to use non-destructive techniques to provide a perfect model for the supramolecular assembly of these biomolecules. This can be successfully achieved by SSNMR which provides high resolution required to study biological materials and deduce the interactions between components at atomic scale resolution [29-31].

Table 1. The identity of the genes removed from different mutants.

Sample name	Gene deleted	Genotype
KU80	Afu2g02620	*CEA17Ku80ΔpyrG+* *CEA17 ΔakuB^{KU80}*
α-1,3-glucan deficient	AfUA_3G00910	*Δags1*
	AfUA_2G11270	*Δags2*
	AfUA_1G15440	*Δags3*
Galactomannan deficient	AFUA_5G02740	*ΔKTR4*
	AFUA_5G12160	*ΔKTR7*
Chitin deficient	AFUA_2G13440	*ΔchsE*
	AFUA_2G13430	*ΔchsEb*
	AFUA_8G05630	*ΔchsF*
	AFUA_3G14420	*ΔchsG*
Galactosaminogalactan deficient	AFUA_3G07860	*ΔGT4C*

Chitin is the component mostly responsible for providing the mechanical strength to the cell wall. This is because it exists as an allomorph, which makes the cell wall thermodynamically more stable by increasing the entropy [32]. The inner core consists of chitin linked to α-1,3-glucan via β-1,3-glucan, which provides the necessary rigidity to the conidia. There are eight chitin synthase genes belonging to two *CHS* families responsible for chitin synthesis in *A. fumigatus* and these are family 1 [*CHSA* (Class I); *CHSB* (Class II); *CHSC* and *CHSG* (Class III)] and family 2 [*CSMA* (Class V), *CSMB* (Class VII), *CHSF* (Class IV) and *CHSD* (Class VI)] (**Table 1.**). The deletion of four genes to study the quadruple mutant Δ*csmA*/*csmB*/*F*/*G* resulted in the production of fungi devoid of Conidia and hyphal growth of 1.3 cm after it had been incubated for three weeks at 37 ^{0}C. The mycelium contained only 30% chitin [33]. Similarly, in *A. fumigatus*, α-1,3 glucans are synthesized by three α-1,3 glucan synthases (Ags1p [AFUA_3G00910], Ags2p[AFUA_2G11270], and Ags3p [AFUA_1G15440]) (**Table 1.**). The simultaneous deletion of all three genes removed α-1,3-glucan completely from *A. fumigatus*. The analysis of the polysaccharide content via alkaline hydrolysis showed that the proportion of the rigid portion to the mobile portion is greater in this mutant sample than the control sample. There was no difference

in mycelium growth in comparison to that of the parental strain. This indicated that α-1,3-glucan did not play any structural role [34]. The removal of *KTR4* & *KTR7* genes (**Table 1**) knocked out galactomannan covalently linked to the β-1,3-glucan, chitin, and α-1,3-glucan core of the cell wall but the galactomannan N or O linked to glycoproteins was retained. Although in the cell wall the removal of galactomannan was compensated by a huge increase in chitin, the fungi had conidium defect. Mycelium growth was also hampered and to add insult to injury the fungi became more sensitive to the drug-Calcofluor White [24]. Δ*GT4C* gene deletion produced *A. fumigatus* exempt from GAG. This exopolysaccharide has virulence and adherence properties which are very important when fungi attack lungs [35].

Previously our research group based on SSNMR data modeled the cell wall architecture, where chitin and α-1,3-glucan together formed the inner hydrophobic scaffolds surrounded by a hydrophilic layer of diversely linked β-glucan and capped by a shell formed by the glycoprotein and the bifunctional molecule α-1,3-glucan [32]. The ongoing research on the fungal cell wall mutation is consistent with previous findings as far as the rigid portion is concerned but in the mobile portion, GAG has been identified along with galactomannan (GM) which was not observed previously by our research group. This makes the current study exciting as it has the potential to unveil many secrets regarding the mobile portion of the *A. fumigatus* cell wall along with changes brought about by the genetic mutation.

During recent times there have been huge developments in SSNMR which enabled the deduction of sub-nanometer packing of carbohydrates, dynamics, and hydration profile in fungal cell wall. We have also witnessed similar development in analysis of cellulose-matrix in plant cell wall as well. This required utilization of isotopically labelled feeding materials which can be expensive. Hence it is important to make way for the advent of a new kind of tool which can

overcome such economical barriers. MAS-DNP method does this work wonderfully well by using of free radicals. This does not come without disadvantages such a signal broadening, radical instability and depolarization [36-38]. Several modifications of polarizing agents have been made to counter such drawbacks [37], Currently it is possible to analyze biomacromolecules using MAS-DNP 2D ^{13}C -^{13}C/^{15}N; which has proven to be a very useful tool in case of labeled materials but could not give any non-diagonal signals for unlabeled materials [32, 36]. This is important specifically for characterization of lignocellulose in plant cell wall, where preparation of labeled materials is time consuming as well as costly. For studies involving extraction of biological materials such as membrane proteins, recent developments in MAS-DNP provided a very convenient way to analyze drug binding sites on the membrane with lesser line-broadening [38, 39]. Hence with consistent development in this field we will be able to reach our goal of removing threshold that prevents analyzing of supramolecular assembly of biomolecules which will help researchers in the field of structural biology.

Chapter 2. A Molecular Vision of Fungal Cell Wall Organization by Functional Genomics and Solid-State NMR

Preparation of Sample

The sample preparation involved using ^{13}C labelled glucose and ^{15} N labelled $NaNO_3$. After preparation of the minimal media, conidia of $5*10^8$ were introduced to the media and left in an incubator for 1.5 days at 37°C and rotation speed of 200 rpm. Conidia belonging to the following strains as mentioned in **Table 1.** of introduction, were introduced separately: wild type strain used in this study was akuB*Δku80* [40]. The α-1,3-glucan deficient strain was the triple mutant with Ags1p, Ags2p and Ags3p encoding genes deleted [34]. The chitin-deficient strain was the quadruple *ΔcsmA/csmB/F/G* mutant in which both chitin synthase family 1 and family 2 genes were deleted [33]. The GM-deficient strain was the double knockout mutant of *KTR4* and *KTR7*, encoding two KTR mannosyltransferases [41] The GAG-deficient strain was the knockout mutant of *gt4c* that encoding GAG synthase [42]. Then the harvested mycelium was recovered by micro cloth filtration and washed using ddH_2O. After this 100 mg of never dried mycelium was analyzed using SSNMR.

Flash frozen mycelium of wild type sample was stored in a -80°C freezer. After grounding mycelium and adding it to 50 ml tubes, the samples was treated with 50 mM Tris, 50 mM EDTA, 2% SDS and 1 mM TCEP and boiled for 20 min to remove protein. Following the separation of supernatant, it was lyophilized and treated with 1 M NaOH in 0.5 M $NaBH_4$ for incubation at 68°C for 1 h modification [43]. The alkali soluble fraction was dialyzed

---

This chapter was previously published as "Chakraborty, Arnab, et al. A molecular vision of fungal cell wall organization by functional genomics and solid-state NMR. *Nature communications* 12.1 (2021): 1-12."

using ddH_2O for 2 days and alkaline insoluble pellets were washed thoroughly with ddH_2O unless pH reached 6. The AI and AS samples were lyophilized and rehydrated for SSNMR analyzed by our collaborators using High Performance Anion Exchange Chromatography (HPAEC) for glucosamine, galactosamine and amino acids whereas neutral sugars were analyzed using Gas liquid chromatography (GLC).

Solid-state NMR experiments

Most of the SSNMR experiments were done using 800 MHz Bruker instrument only ^{13}C T_1 relaxation, ^{13}C DIPSHIFT, 1D water-edited experiment, ^{13}C INEPT and ^{13}C-^{13}C RFDR experiments were run using Bruker 400 MHz instrument. The experiments were run using radio frequency field strength between 62.5-83.3 KHz in the ^{1}H channel. Similarly, 50-62.5 KHz field strength was used for ^{13}C channel and 41,5 KHz was used for ^{15}N channel. The ^{13}C resonance data were collected on TMS scale and externally referenced using Met Cδ of a model peptide N-formyl-Met-Leu-Phe-OH (f-MLF) at 14.0. The data obtained have been processed using the following methods: TopSpin, Microsoft Excel, OriginPro, and Adobe Illustrator [44].

The initial identification of polysaccharides and proteins were done using 1D ^{13}C CP followed by 2D ^{13}C-^{13}C CORD for the rigid polysaccharides in the cell wall [45, 46]. Mobile polysaccharides were characterized by 2D ^{13}C DP J-INADEQUATE experiments after initial screening using 1D ^{13}C DP. Both 1D ^{13}C DP and 2D ^{13}C DP J-INADEQUATE were run at 2s recycle delay which selectively analyzed mobile molecules [47, 48]. Further confirmation of chitin and other rigid proteins were done using 2D ^{13}C-^{15}N NCA(CX) heteronuclear correlation spectrum with a 5 ms ^{15}N-^{13}C CP and a 15 ms or 100 ms PDSD mixing time [49]. All of these data were collected with magic angle spin (MAS) speed of 10 KHz. Additional analysis for rigid

polysaccharides in alkali soluble (AS) and alkaline insoluble (AI) polysaccharides were done using 2D SPC5 dipolar-INADEQUATE spectrum [50] with ^{13}C CP and 2D ^{13}C-^{13}C radio frequency-driven recoupling (RFDR) with a recoupling time of 1.5 ms [51]. These data were run at MAS frequency of 7.5 KHz. The composition analysis of the rigid polysaccharides was done by determining the average volume of cross-peaks from by 2D ^{13}C-^{13}C CORD and for mobile molecules we took the average volume of spin pairs belonging to individual polysaccharides [52, 53].

The integration function of Bruker Topspin software was used to determine the peak volumes in the 2D spectra. The assignment of the cross peaks and the peak volumes are given in **Supplementary Tables A.3.** and **A.4.** The peaks at C6 are generally skipped during composition analysis because they contain overlapping region. Exception is the case of α-1,3-glucan, where the peak intensity of the closely placed signals of the C2 (71.9 ppm) and C4 (71.7 ppm) are summed and divide equally. The relative abundance of a specific polysaccharide ($RA^{poly.x}$) was calculated by normalizing the sum of integrals by the number of peaks using the following equation:

$$RA^{poly.x}(\%) = \frac{\sum_{n=1}^{n_{peaks}^{poly.x}} I_n^{poly.x} / n_{peaks}^{poly.x}}{\sum_{m=1}^{m^{poly.}} (\sum_{n=1}^{n_{peaks}^{poly.x}} I_n^{poly.x} / n_{peaks}^{poly.x})} \times 100$$

where $n_{peaks}^{poly.x}$ is number of cross-peaks and $I_n^{poly.x}$ is integral of peak volume.

The standard error of a specific polysaccharide ($std.ERR^{poly.x}$) was determined using the standard deviation of integrated peak volume dividing by square summation of the number of cross-peaks. The total standard error ($\sum std.ERR$) calculated by square sum of the standard error of each polysaccharide. Then remaining calculations are done as shown below.

$$ERR^{poly.x} = \frac{std.ERR^{poly.x}}{\overline{x}^{V^{poly.x}}} \times \frac{\sum std.ERR}{\sum V^{poly.}} \times RA^{poly.x}$$

For dynamics analysis ^{13}C T_1 relaxation data collected were plotted in Origin Pro. The experiment was basically a series of 2D ^{13}C-^{13}C CORD using variable z-filter 0 s, 0.2 s, 1s, 3s and 8s. It was conducted at 298 K and MAS speed of 10 KHz. The data were fit using single exponential decay. Hydration of rigid polysaccharides was analyzed using ^{1}H-T_2 relaxation filter of 0.6 ms × 2, which removed 90% of carbohydrate magnetization but retained 80% of water magnetization, details of this experiment entail 0.1 µs to 64 ms ^{1}H-T_2 mixing time followed by ^{1}H-^{13}C CP to ensure high-resolution of ^{13}C. The buildup curves were analyzed using single exponential growth equation [54]. The DIPSHIFT spectra of the wild type and alkaline treated samples were collected using radio frequency of 62.5 kHz for ^{13}C channel and within 62.5-83 kHz for ^{1}H channel. These spectra were collected at MAS of frequency 7.5 KHz [55].

Transmission electron microscope measurement (TEM)

The TEM images were acquired after placing the sample on a glow discharged TEM grid for some time and then staining it with a mixture of 2% uranyl acetate and lead citrate solution. The device used to collect TEM images was JEOL JEM-1400 electron microscope. The cell wall thickness was analyzed using ImageJ software after calibrating the bar scales and then statistical analysis was done via unpaired student t-test [54].

Polysaccharide structure and a new vision of their role in the organization of the cell wall

Comparison of these samples allowed us to evaluate the contribution of each polysaccharide to the structure and function of fungal cell walls. The cell wall (**Supplementary Fig.A.1.)** thickness has been reduced in all four mutants, with the thinnest wall (only 110 nm on average) (**Supplementary Fig.A.2.)** observed in the chitin-deficient mutant **(Supplementary Fig.**

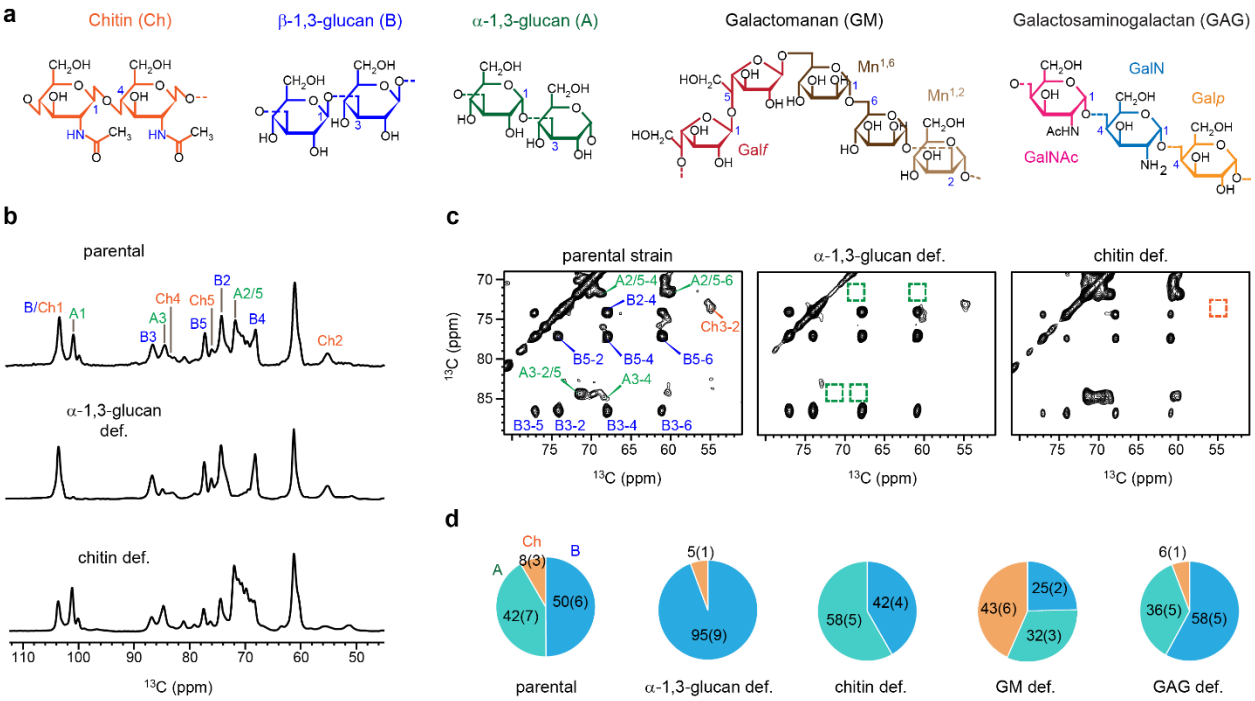

Figure 2.1. **Structural changes in the rigid core of A. fumigatus mutant cell walls. a** Representative structure of fungal carbohydrates. Abbreviations are shown for different polysaccharides and sugar units. **b** 1D ^{13}C–CP spectrum showing different intensities for rigid polysaccharides. Abbreviations are used for resonance assignments. For example, A1 denotes α-1,3-glucan carbon 1. Ch and B represent chitin and β-1,3-glucan, respectively. **c** 2D ^{13}C–^{13}C correlation spectrum with 53 ms CORD mixing detecting intramolecular cross peaks. For example, B3-5 is the cross peak between β-1,3-glucan carbon 3 and carbon 5. The missing peaks of α-1,3-glucan and chitin in two mutants are highlighted using dash line boxes. **d** Estimation of polysaccharide composition in the rigid portion of cell walls. Chitin, α-1,3-glucan, and β-glucans are shown in orange, green, and blue, respectively. The percentage values represent the molar fraction of rigid polysaccharides as estimated using the integrals of cross peaks in 2D CORD spectra, which is detailed in Supplementary Table A.3. Standard errors included in the parentheses are based on data presented in Supplementary Fig. A.3 and computed as described in the Supplementary Methods. *Source*: The entire panel was adapted from reference (54), an open-access article.

A.2. and Table A.2.) peak of chitin carbon 2 (Ch2) at 55.5 ppm faded in the chitin-deficient sample owing to its partial. After harvesting uniformly ^{13}C, ^{15}N-labeled samples by growing the five strains for 1.5 days using minimal medium containing ^{13}C-glucose and ^{15}N-$NaNO_3$ at 37°C.Then intact cells were packed in the MAS rotor, retaining its native environment. The rigid domain of cell walls was selectively detected using one-dimensional (1D) ^{1}H-^{13}C cross polarization (CP)

spectra (**Fig. 2.1.b**). Only three polysaccharides were found to constitute the rigid core, including chitin, α-1,3-glucan, and β-1,3-glucans. All the key peaks of α-1,3-glucans, for example, carbon 1 at 101 ppm (A1) and carbon 2/5 at 72 ppm (A2/5), were absent in the α-1,3-glucan deficient mutant. Similarly, the resolved overlap with protein and lipid peaks (**Supplementary Table A.1.**). The absence of signature peaks confirmed the exclusion of α-1,3-glucan and chitin in the cell walls of their corresponding mutants.

The absence of the rigid polysaccharide (chitin and α-1,3-glucan) peaks from the corresponding mutant samples indicated their disappearance from the rigid portion of the cell wall (**Fig. 2.1.c**). The quantitative analysis of the 2D ^{13}C-^{13}C CORD spectrum done as mentioned in the method section provided the relative percentage of α-1,3-glucan, β-1,3-glucan, and chitin in all samples (**Fig. 2.1.d**). These data were of high resolution with full-width at half-maximum (FWHM) being between 0.45-0.775 ppm for rigid macromolecules (**Supplementary Fig. A.3.**). In the wild type sample, the percentages of β-1,3-glucan, α-1,3-glucan, and chitin were 50%, 42%, and 8%, respectively (**Fig. 3.1.e**). The complete removal of chitin from the chitin deficient sample changed the percentage of α-1,3-glucan to 58% making it the major rigid polysaccharide component of the cell wall. The α-1,3-glucan deficiency was compensated by a huge increase in β-1,3-glucan to 94% whereas the galactomannan deficiency increased chitin amount to 43% (**Supplementary Table A.3.)**. There was no change observed in the rigid portion of the GAG deficient mutant sample. Possibly because GAG had no role to play in the rigid portion of the cell wall.

The unambiguous determination of galactomannan, α-1,3-glucan, β-1,3-glucan, and galactosaminogalactan with a narrow range of FWHM of 0.4-0.6 ppm (**Supplementary Fig. A.4.**) from the polysaccharide region of 2D ^{13}C DP J-INADEQUATE spectrum showed that the mobile

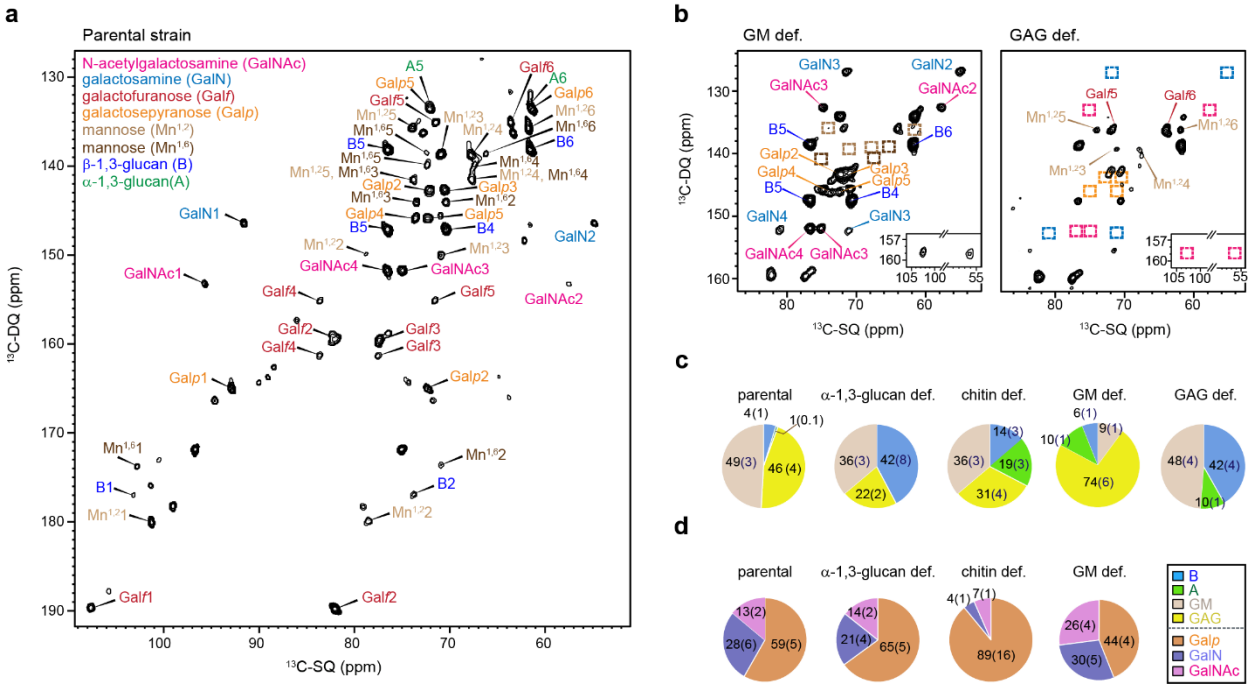

Figure 2.2. **The mobile domain of *A. fumigatus* cell wall is rich in GM and GAG**. **a** ^{13}C DP J-INADEQUATE spectrum resolving the carbon connectivity for each polysaccharide. Abbreviations are used for resonance assignments and different polysaccharides are color-coded. **b** Comparison of mobile polysaccharides in GM- and GAG-deficient mutants. Missing peaks of GM and GAG are highlighted using dash line boxes (typically, brown for mannose, orange for galactopyranose, cyan for galactosamine, and magenta for N-acetylgalactosamine). Insets show the signals of GalN'/GalNAc residue in the GM-deficient mutant. **c** Molar fractions of mobile polysaccharides in each cell wall sample estimated from peak volume. **d** Monosaccharide compositional changes of GAG observed in the four samples. Standard errors are included in parentheses. The numbers in the pie charts shown by (c, d) are molar percentages as detailed in Supplementary Table A.4. The numbers in the pie charts are percentage values. *Source*: The entire panel was adapted from reference (54), an open-access article.

region of *A.fumigatus* is very dynamic. GAG consists of sub-components, which combine randomly to form trisaccharides and disaccharides [56]. This is evident from the chemical shift of C1 which is 93.2 ppm, 91.7 ppm, and 95.7 ppm for galactose, galactosamine, and N-acetylgalactosamine respectively (**Fig. 2.2.a**). Just like chitin, N-acetylgalactosamine and galactosamine have characteristic C2 chemical shifts below 60 ppm that is a signature for C-N

bonds in that position. In the GM deficient mutant sample, the amount of galactomannan reduces from the mobile portion but is not completely removed. The GM and GAG peaks were determined by missing signals of their monosaccharide units α-1,2-mannose ($Mn^{1,2}$) and α-1,6-mannose ($Mn^{1,6}$) for GM and galactopyranose (Gal*p*), galactosamine (GalN), and N-acetylgalactosamine (GalNAc) for GAG (**Fig. 2.2.b**), in their respective deficient sample, The deficiency of galactomannan is compensated by an increase in galactosaminogalactan in the mobile region. GAG is completely removed from the GAG-deficient mutant sample and it is followed by a significant increase in β-1,3-glucan to 42% and β-1,5-galactofuranose to 33% in the mobile portion (**Fig. 2.2.c**) as can be seen from the composition analysis of mobile components, which was done by taking the cross peak integrals from 2D ^{13}C DP J-INADEQUATE spectrum. One of the interesting facts about the two most heterogeneous mobile region polymers GM and GAG is that they vary in composition with genetic mutation (**Fig 2.2.d**). In case of GAG, Gal*p* seemed to be most dominant component in all mutants (around 60-90%) except GM deficient mutant where the distribution was even (**Supplementary Table A.4.**). These results were supported by chromatographic studies (**Supplementary Fig. A.6.**).

The fungal cell wall mutations result in compositional changes both in the rigid and the mobile portion. This also changes the sub-nanometer packing in the inner core of the cell wall as well as the outer hydrophilic layer of the rigid portion. Along with polysaccharides, the protein composition and mobility also change that can be an indication of possible linkages between mobile portion polysaccharides and proteins. Further studies are necessary to confirm these findings.

Delicate difference exists between the two types of galactose units in the mobile polysaccharides. Structurally, both Gal*f* and Gal*p* have 6 carbons, however, the former has a 5-

membered ring and a unique C1 chemical shift at 108 ppm while the latter has a 6-membered ring (**Fig. 2.1.a**). Functionally, Gal*f* is branching GM with proteins and inner cell wall polysaccharides, whereas Gal*f* is part of GAG backbones [41, 57].

Alkaline dissolution of polysaccharides

Apart from comparison of analysis of different genetic mutants we have also analyzed the wild type fungi after treating it with 1M NaOH and heating it at 65°C. The hot alkaline separated polysaccharides based on their alkaline solubility with β-1,3-glucan and chitin being inert to hot alkali whereas α-1,3-glucan was present in both AI and AS fraction. Just like whole cell analysis 1D ^{13}C CP spectra selectively detected rigid polymers in both the fractions. This was followed by 2D ^{13}C-^{13}C CORD experiment which gave the composition of rigid portion of AI to be 57% β-1,3-glucan and 27% chitin. The presence of α-1,3-glucan has been confirmed in both phases via overlapping signals in 2D ^{13}C-^{13}C CORD (**Fig. 2.3.a**). This changes previously held idea that α-1,3-glucan was not involved in formation of fibrils alongside chitin and β-1,3-glcuan. These results were further confirmed by failure to remove α-1,3-glucan even after repeated alkaline treatment (**Fig. 2.3.b and Supplementary Fig. A.7.**).

The spectra selectively detecting mobile carbohydrates showed additional set of peaks from β-1,3-glucan and chitin for AI fraction, while for AS it exhibited unique signals of α-1,3-glucan (**Fig. 2.3.c**). The presence of chitin in the mobile phase, although with relatively low content, is unexpected. This observation indicates the presence of structurally disordered chitin domains (though with a very small population) that are associated with matrix polymers, for example, β-1,3-glucans [58]. Both AI and AS samples showed signals from the mannose and Gal*f* residues of GM. These results were supported by chromatographic studies as mentioned in the method section however slight discrepancies do exist. SSNMR (can give the distribution of

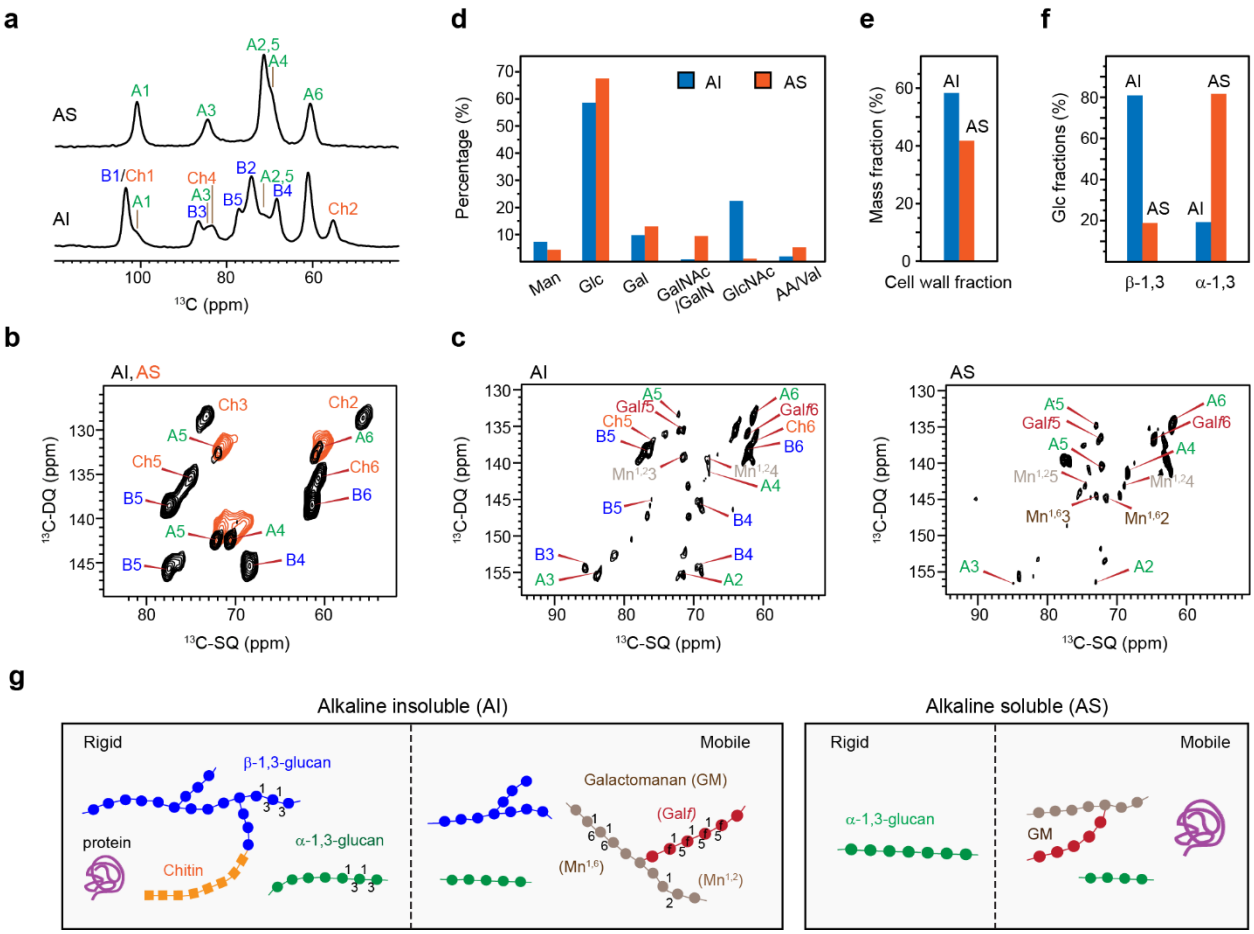

Figure 2.3. **α-1,3-glucan is present in both alkali-soluble and insoluble fractions of the parental sample**. **a** 1D ^{13}C CP spectra detecting the rigid molecules in the alkali-soluble (AS) and alkali-insoluble (AI) fractions of the parental sample. **b** Overlay of 2D ^{13}C CP dipolar-INADEQUATE spectra showing the rigid molecules in the alkaline-soluble (AS, orange) and alkaline-insoluble (AI, black) portions of A. fumigatus cell walls. Signals of α-1,3-glucans, such as A4, A5, and A6, are present in both portions. **c** ^{13}C DP J-INADEQUATE spectrum showing the mobile polysaccharides in the alkali insoluble (left) and soluble (right) parts. **d** Compositional analysis of both AI (blue) and AS (orange) fractions obtained by GC-HPLC and enzymatic degradation. The x-axis reports different monosaccharide units as well as the amino acids (AA) or valine (Val). **e** Relative mass percentages of the AI and AS fractions. **f** Relative fractions of β-1,3-glucan and α-1,3-glucan. **g** Summary of polysaccharides and proteins identified in both rigid and mobile portions within the alkali insoluble and soluble fractions. *Source*: The entire panel was adapted from reference (54), an open-access article.

polysaccharides in mobile and rigid portion separately (**Supplementary Table A.5.**) but how polysaccharides are packed together induces some errors which are difficult to quantify.

Sometimes incompatibility of the domain in which carbohydrates exist prevents its detection via SSNMR as in the case of GAG: whose signature peaks (for example, the carbon 2 peaks at 52-55 ppm) remained invisible in both AI and AS sample although chromatographic studies confirmed its presence (**Supplementary Fig. A.6. and Table A.6.**). These findings allow us to summarize the partitioning of polysaccharides in four phases: the rigid and mobile domains of AI and AS portions (**Fig. 2.3.d**). β-1,3-glucan spans across the rigid and mobile phases of AI fractions while chitin mainly exists in the rigid phase of AI materials. GM remains highly dynamic. The rigid domain of AS portion is dominated by α-1,3-glucan but this molecule also exists in all the other three phases: the distribution heterogeneity is an indicator of its functional complexity. Protein signals were mainly observed in the mobile phase of AS molecules (**Supplementary Fig. A.8.**), together with a small portion in the rigid phase of AI components, which will be explained below.

Protein-carbohydrate association in fungal cell walls

Fortunately, ^{15}N labeling enabled measurement of the 1D ^{15}N spectrum along with 2D ^{13}C-^{15}N correlation spectrum which showed the ability of chitins to form diverse crystalline structures that change depending on the cell wall polysaccharide deficiency. It also showed the hydrophobic proteins that prevent the penetration of moisture into the fungal cell wall [59]. this was evident from the two amide peaks at 124 ppm and 129 ppm, together with an amine peak at 38 ppm. The NC correlation spectrum of the chitin deficient sample had no chitin peak, and it even did not show any peaks corresponding to GAG for any strains. GM deficient and GAG deficient samples had broader chitin peaks than the control sample. This indicated that the chitin formed more allomorphs in these samples than in the control (**Fig. 2.4.d**). Hence the cell wall strength increased with GAG

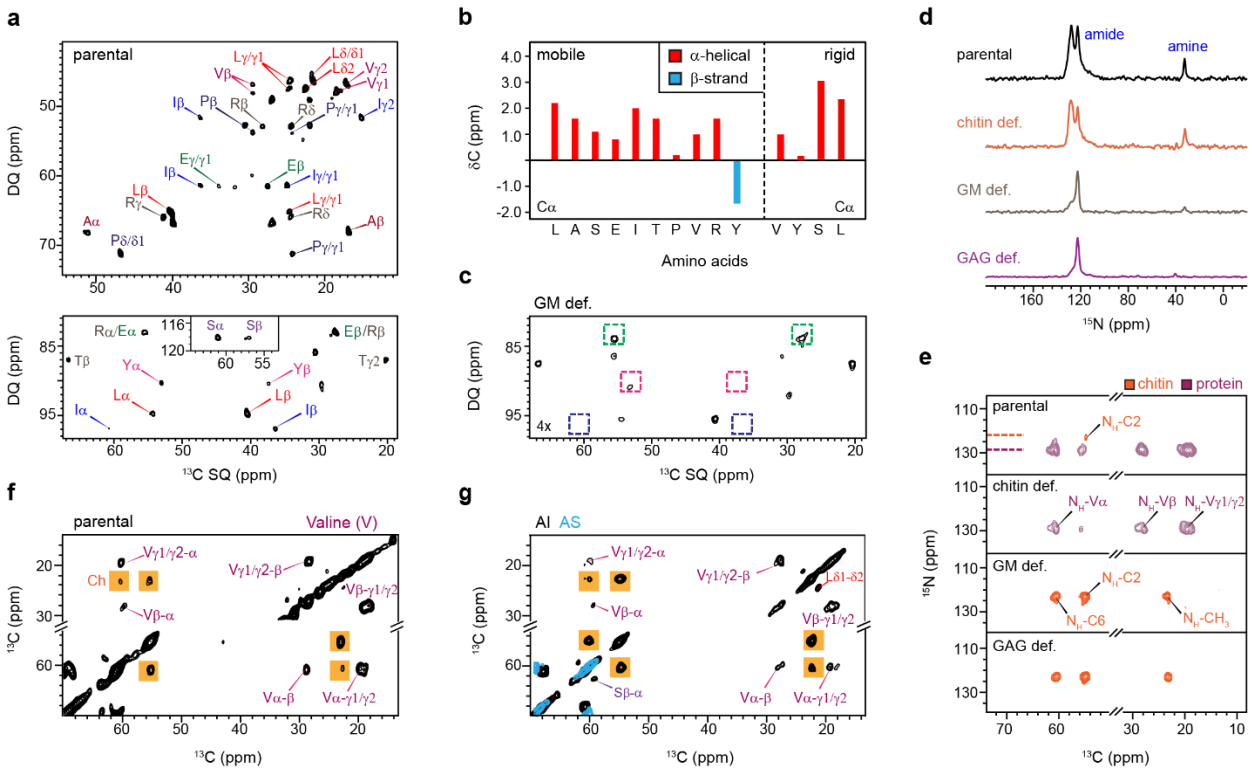

Figure 2.4. **Structural assembly of glycoproteins in fungal cell walls**. **a** 2D ^{13}C DP J-INADEQUATE spectrum detecting the amino acids of mobile proteins. The assignments represent the amino acid types and carbon sites. For example, A_β represents the carbon-β of alanine. The inset shows the signals of Serine. **b** Backbone ^{13}C chemical shifts suggest the dominance of α-helix secondary structure in both mobile and rigid phases of proteins. **c** Removal of galactomannan results in protein depletion indicated by the decline in amino acid signals as highlighted using dash line boxes. **d** 1D ^{15}N CP spectra showing multiple amide and amine signals from cell wall polysaccharides and proteins. The ^{15}N signals vary in the parental sample and mutants. **e** 2D ^{15}N-^{13}C correlation spectra showing the chitin (orange) and protein (purple) signals. Chitin signals are missing in the chitin-deficient. Rigid proteins are absent in the GM-deficient and GAG-deficient samples. **f** Valine is the major rigid amino acid in whole cells of the parental sample as shown by the 2D ^{13}C-^{13}C CORD spectrum. Chitin signals are shown in yellow boxes. **g** Valine is preserved in the rigid portion of alkali-insoluble (AI) part but becomes absent in the alkali-soluble (AS) fraction. *Source*: The entire panel was adapted from reference (54), an open-access article.

and GM deficiency. However, there are no rigid proteins in GAG and GM deficient samples making them more moisture sensitive.

The analysis of the mobile proteins using ^{13}C DP J-INADEQUATE spectrum confirmed the presence of ten amino acids (**Fig. 2.4.a and Supplementary Fig. A.9.**). The high sensitivity of protein backbone chemical shifts to φ and ψ torsion angles makes it a useful tool for probing

the secondary structure [60]. The Cα and CO chemical shifts revealed strong α-helicity of most residues except for tyrosine (**Fig. 2.4.b**). Proteins got completely removed from the GM deficient sample (**Fig. 2.4.c** and **Supplementary Fig. A.10.**). We anticipated that the justifications to this could be related to glycoprotein linkages in the mobile portion of the cell wall. The J-coupling-based refocused ^{13}C INEPT (Insensitive Nuclei Enhanced by Polarization Transfer) using short recycle delay showed proteins that were loosely bound to peptides and highly mobile. The GAG deficient sample had proteins making a transition to the highly mobile region (**Supplementary Fig. A.10.**) which was not observed in the case of GM deficient and wild type sample. Therefore, we conclude that galactomannan is very important for protein stability.

Strikingly, the protein region of 2D ^{15}N-^{13}C spectra mainly has valine (V) signals (**Fig. 2.4.e**), with only a minor contribution from other amino acids. These peaks were observed at 124ppm and 129 ppm belonging to its amides. This unexpected finding was verified by the strong valine cross peaks observed in the aliphatic region of the 2D ^{13}C-^{13}C correlation spectrum (**Fig. 2.4.f**). The same signals were fully retained in the alkali-insoluble portion of cell walls but disappeared in the alkali-soluble fraction (**Fig. 2.4.g**). These three observations consistently show that valine might be involved in the formation of rigid polysaccharide complex and playing a role in holding together these molecules. This key association remains unaffected after alkali treatment (**Supplementary Fig. A.7.**).

Polymer dynamics and hydration in the mutants

The heterogeneous molecular mobility profile obtained from the pseudo-3D ^{13}C T_1 relaxation experiments **(Supplementary Fig. A.11.)** that probe local reorientation [32] suggested the

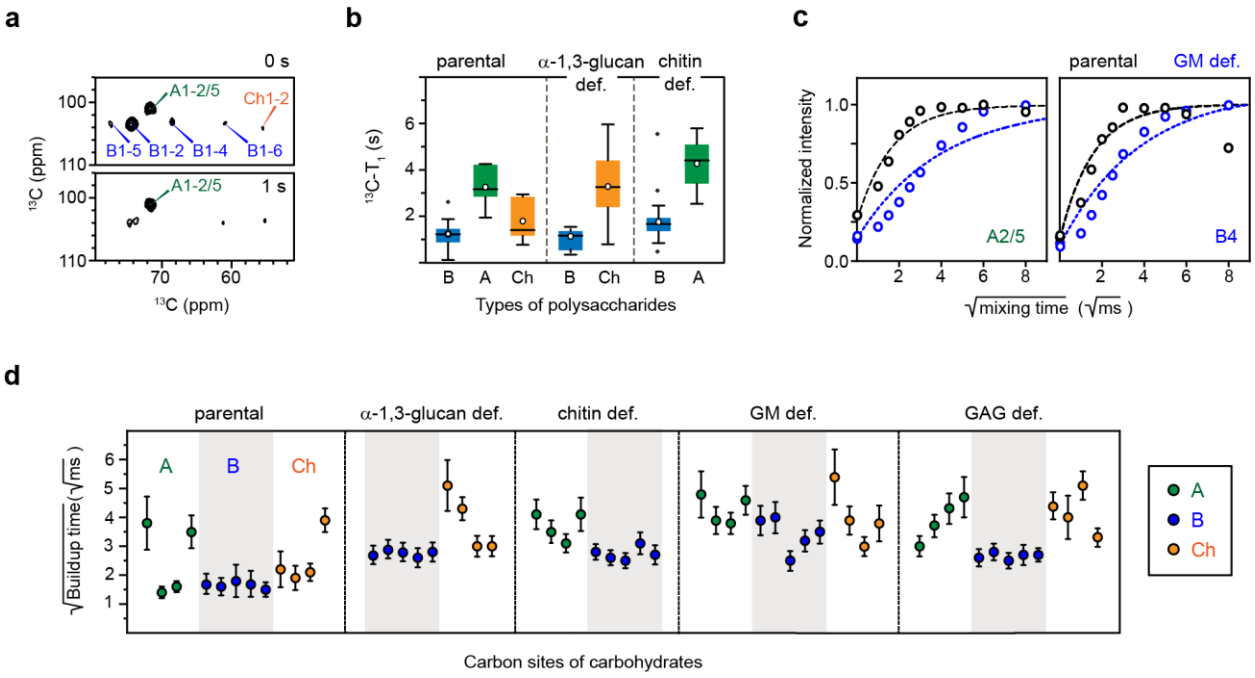

Fig. 2.5. **Modulated dynamics and water contact of polysaccharides in A. fumigatus mutants**. The NMR data of β-1,3-glucan (B), α-1,3-glucan (A), and chitin (Ch) are plotted in blue, green, and orange, respectively. **a** Representative 2D ^{13}C–^{13}C spectra with 0 s (top) and 1 s (bottom) z-filter time for measuring ^{13}C–T_1 relaxation. Signals of α-1,3-glucans are effectively retained after 1 s, indicating the slow ^{13}C–T_1 relaxation of this polysaccharide. **b** Box and whisker diagram plotting the ^{13}C T_1 relaxation time constants of β-1,3-glucan (B; n = 19), α-1,3-glucan (A; n= 6), and chitin (Ch; n = 13) for parental and mutant samples. The box starts from lower quartile to upper quartile, with the horizontal bar and the open circle presenting the median and mean, respectively. The length of the whiskers is determined by the product of 1.5 and interquartile range, with outliers shown as separate dots. **c** Representative buildup curves for the water-edited spectrum of parental (black) and GM-deficient (blue) samples. **d** Data representing the buildup time constants that reflect the degree of water retention at various carbon sites of different polysaccharides. Time constants for β-1,3-glucan (n = 5), α-1,3-glucan (n = 4) and chitin (n = 4) are generated from the fit to exponential function. Each point reflects the best-fit value for buildup time constant ± s.e. Shaded area represents the data of β-1,3-glucan. The data plotted in (b, d) are summarized in Supplementary Tables A.8, A.9, respectively *Source*: The entire panel was adapted from reference (54), an open-access article.

existence of different polysaccharide matrixes within the rigid portion of the fungal cell wall (**Fig. 2.5.a** and **Supplementary Table A.7.**). The change in molecular mobility profile owing to genetic mutations also echoed the removal of rigid polysaccharides from their corresponding mutants. The average relaxation times for α-1,3-glucan, β-1,3-glucan, and chitin were 3.2 s, 1.8 s, and 1.2 s, respectively (**Fig. 2.5.b**) in the wild-type sample. The chitin got rigidified in the α-1,3-glucan

deficient mutant sample, with the relaxation time rising to 3.3 s for chitin whereas the β-1,3-glucan became more mobile. However, in the chitin deficient sample both α-1,3-glucan and β-1,3-glucan became less mobile with their relaxation times rising to 4.3 s and 1.8 s. The relaxation profiles of chitin indicated that it existed as an allomorph just like it had been mentioned in the previous work [32]. The distribution of relaxation times for all components changed with the genetic mutation. All this information indicated that the packing in the polysaccharide matrix of α-1,3-glucan, β-1,3-glucan, and chitin changes with genetic mutations.

We probed the change in packing via water-to-polysaccharide ^{1}H polarization transfer experiment [61, 62]. Here ^{1}H-T_2 relaxation filter removes polysaccharide magnetization but the length is not long enough for the magnetization of water undergoes negligible decay. Then the transfer of water ^{1}H polarization to carbohydrates selectively intensifies signals of polysaccharides in the vicinity of water molecules. The time required for signals to reach equilibrium can be used as a quantitative indication for the distance between water molecules and individual caron sites (**Supplementary Fig. A.12.** and **Table A.8.**). The polysaccharide intensity equilibration time in the GM-deficient sample is greater than in the parental fungus, revealing that polysaccharides in the wild type strain is surrounded by more water molecules than in the GM deficient mutants (**Fig. 2.5.c**).

Comparing all the mutants it was observed that α-1,3-glucan and chitin has longer retention times than β-1,3-glcuan (**Fig. 2.5.d**). This is mainly because α-1,3-glucan and chitin forms hydrophobic scaffold in most strains except the ones where they are dispensed and part of β-1,3-glucan fulfils that role. Generally, polysaccharides have been found to lose its ability to retain water molecules with genetic mutation. This can be because for having maximum water retention

capacity the cell wall must have appropriate relative proportion of α-1,3-glucan, chitin and β-1,3-glcuan. Significant changes took place in the galactomannan-deficient sample (**Fig. 2.5.c**).

The examination of protein region and hydration of polysaccharides showed that GM deficiency cause significant changes to both inner cell wall packing and outer cell wall protein layer. This is also consistent with previous studies which showed reduced growth, less conidiation, higher germination, and more obviously abnormal polarity growth [41].

The $^{13}C–^{1}H$ dipolar couplings data obtained via dipolar chemical shift correlation experiment (DIPSHIFT) indicates how motional amplitude of polysaccharides changes after alkaline treatment[55]. The high order parameters of β-1,3-glucan in the control sample indicates it is firmly held in its domain. However, nothing concrete can be mentioned about the domain where chitin and α-1,3-glucan exists (**Supplementary Fig. A.13. and Table A.9.**). C3 and C5 of chitin had vastly different order parameter than C2 and C4. Even though chitin forms allomorphic structures, which can possibly explain such anomalies, likewise α-1,3-glucan is present in mobile portion and rigid portion of the cell wall provides some rationalization but does not solve the conundrum. There can be other reasons too, since DIPSHIFT probes CH bond motions of individual monomer units, there can also be glycoprotein linkages present alongside C atoms with greater dipolar dephasing. These data do not blend well with pseudo 3D ^{13}C T_1 relaxation data which mostly probes motion of polymer segments. After alkaline treatment β-1,3-glucan and chitin mobilizes with order parameter dipping. This is because alkaline treatment removes α-1,3-glucan increasing its motional amplitudes. Unfortunately, the increase in order parameter of α-1,3-glucans in the alkaline soluble fractions are a mismatch with what is expected. This may be indication of variable polymer matrix in control, AI and AS samples. Simply our original definition of rigid and mobile report during former research work has seriously been called into question.

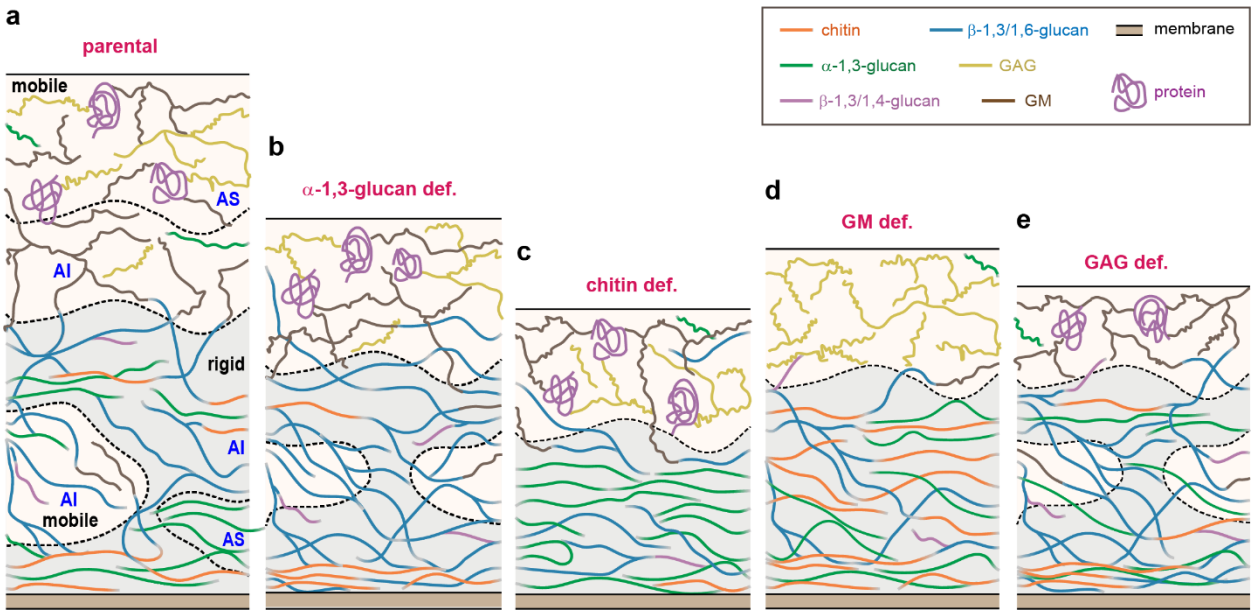

Figure 2.6. **Structural scheme of fungal cell walls substantiated by NMR data and mutant strains. For each sample, the mobile and rigid phases are highlighted in pale yellow and pale blue, respectively. a** Cell walls of the parental sample, with the alkali-soluble (AS) and alkali-insoluble (AI) portions labeled. The rigid and mobile portions of AI and AS are also shown. The molar fractions of the rigid and mobile domains from solid-state NMR have been considered, but the scheme may not be strictly to scale. The molecule types are labeled and color coded. Templated from the parental cell wall, schematic illustrations are also shown for the four mutants devoid of (**b**) α-1,3-glucan, (**c**) chitin, (**d**) GM, and (**e**) GAG, with the major changes shown. The cell wall thickness is proportional to the average value of each strain observed by TEM, but a broad distribution of thicknesses was observed in Supplementary Fig. A.2. *Source*: The entire panel was adapted from reference (54), an open-access article.

Discussion

Current findings using high resolution Solid-state NMR challenges previous understanding regarding the structure of *A. fumigatus* cell wall. The parental *A. fumigatus* cell wall is composed of an outer shell and an internal domain (**Fig. 2.6.**). The highly mobile outermost layer contains GAG, GM, proteins, as well as a small amount of α-1,3-glucans. The inner domain comprises of a highly stiff and hydrophobic complex of α-1,3-glucan and chitin, which is distributed in a soft

and hydrated matrix of β-glucans. Chitin, α-1,3-glucan, and β-glucans are joined together, probably by covalent linkages, forming fibrils which are resistant to hot alkali treatment. Portion of the α-1,3-glucan is involved in fibril formation with β-1,3-glucan and chitin while the rest remain far away hence they are extractable via alkaline treatment.

Distinguishing changes in spectral properties with genetic mutation it is possible to figure out the way fungi adopt to depletion of polysaccharides. The removal of α-1,3-glucan, GM and GAG brings about a decrease in cell wall thickness (115-135 nm instead of 206 nm for the parental walls). The deficiency of α-1,3-glucan can be easily made up by increasing β-13-glucan in the inner cell wall (**Fig. 2.1.e**). Its absence rigidifies chitin (**Fig. 2.5.b**) in the inner cell wall as α-1,3-glucan usually consumes extra space. The removal of GM increases the chitin content five- fold. Since chitin has the capacity to form multiple hydrogen bonds owing to the presence of carbonyl and amide group, thermodynamic stability of the cell wall increases which is directly brought about by increase in entropy. This phenomenon is strengthened by the fact that chitin deficient sample undergoes huge amount of cell wall perturbation reflected in the high standard deviation of the cell wall thickness data (110 ± 90) (**Supplementary Table A.2.**). The reduction in GM removes most of the proteins from the GM deficient fungi meanwhile removal of GAG exposes more β-1,3-glucan to the human immune system. The hydrogen bonds on chitin structure also makes it hydrophobic and hence in GM deficient sample the cell wall polysaccharides have higher retention time (**Supplementary Table A.8.**).

Overall, it was observed that fungi follow some basic rules to recover from lost polysaccharide. These goes as follows: the reduction in one polysaccharide brings about increase in the others which also brings about change in packing, hence change in rigidity and hydration.

The hydration reduces but rigidity can go either way depending on which polysaccharide went missing. These changes help fungi to grow amidst condition that are not too conducive for its vegetation. However, in some cases like GM deficiency makes it irrecoverable for fungi as they lose water (**Fig. 2.5.d**) uptake ability as well as proteins needed for enhancing its stability [63].

In this study we have observed for first time two crucial pieces of information regarding glycoproteins which are synergistic. The GAG deficiency increases protein mobility as GAG is well-known for its adhesive ability in the outer cell well region. Similarly, valine cannot be removed by alkaline treatment, and it is retained with the inner cell wall polysaccharide in the AI fraction, which indicates it forms a connection between inner cell wall glycoproteins and outer cell wall GAG (**Fig. 2.4.f, g**) [35, 64]. GPI-anchored galactomannoprotein Mp1 has been identified as a specific cell wall protein, while GPI-anchored Ecm33 and Gel1 are membrane proteins whose degraded fragments were found in cell wall [65]. The high content of valine residues in these proteins (5.3-6.7%), and in particular, their large number in the GPI-signal domain (12-21%), provide indirect support to the putative function of valine in stabilizing polysaccharide-protein association (**Fig. 2.4.g**).

This exploratory study has established the structural foundation for further investigating the ultrastructure of cell walls in the large collection of fungal strains, including those showing high virulence or drug resistance. A molecular-level understanding of how cell walls structurally respond to antifungal treatments may guide the design of compounds with improved efficacy to combat invasive fungal infections.

Chapter 3. Biomolecular Complex Viewed by Dynamic Nuclear Polarization Solid-State NMR Spectroscopy

Introduction

Heretofore SSNMR has proven to be quite useful when it comes to detecting biomolecules and providing abstract image of its biomolecular assembly. They were mainly used for studying amyloid fibrils, membrane proteins, large protein-protein complex, ion channels and transporters, and nucleic acids [66-71]. However, high-resolution studies of biomolecules have been far outreach using SSNMR. This is mainly because their native environment is heterogeneous with extremely low concentration of the analyte of interest. The sensitivity-enhancing DNP technique combined with special labeling methods and spectral editing have proven to be pretty useful in the past 10 years to study the protein folding, biopolymer interactions, and ligand binding using the intact cells of humans, bacteria, plants, and fungal pathogens, as well as intact virus [32, 72-76]. This study will protract how several new applications to cellular samples or bio-composites. It also links the structural restraints to conceptually comprehend the supramolecular architecture of biological constructs, which in the long run have the ability to improve therapeutic agents, biopolymer-based materials, and bio renewable energy.

This chapter was previously published as "Chakraborty, Arnab, et al. Biomolecular complex viewed by dynamic nuclear polarization solid-state NMR spectroscopy. *Biochemical Society Transactions* 48.3 (2020): 1089-1099".

DNP enhancement of sensitivity enables new research avenues

NMR has very low sensitivity because of the low gyromagnetic rat ion of most NMR active nuclei. DNP predominantly uses unpaired electrons (high gyromagnetic ratio) specially from This chapter radicals (**Figure 1.A**) incorporated into appropriate site by physical or chemical means to transfer its own polarization to the ^{13}C or ^{1}H nuclei [77-79]. This polarization transfer is aided by microwave spectroscopy. The sensitivity enhancement is determined by comparing the signal intensity after turning on the microwave to that, before turning it on. There is another factor depolarization effects, which has to be taken into account as well for better assessment [37]. The stringent requirement of chemical stability and long NMR relaxation times impose alongside obtaining maximum sensitivity imposes a constraint on to temperature rang at which these experiments are feasible. Typically, it is in the range of 90-110 K. These unfortunately leads to large line-broadening due to longer time specific conformation of biopolymers can be retained. Special care must be given to the choice of materials used to prepare DNP juice because this impacts DNP efficiency depending on how radicals are dispersed and interacting within the biological[80, 81]. Different types of water-soluble bi-radicals (with two unpaired electrons), such as TOTAPOL and AMUPol [82, 83], have been widely used (**Fig. 3.1.B,C**). In recent times a promising asymmetric biradical AsymPolPOK has proven to be pretty useful due to smaller DNP buildup time and doubling sensitivity enhancement ratio when compared with the commercial radicals (**Fig. 3.1.D**) [84]. Apart from these researchers are desperate to use radicals covalently bonded to biomolecules which bars water exposure. This is useful specially when studying membrane proteins, or specifically probe biomolecular interaction sites [85, 86].

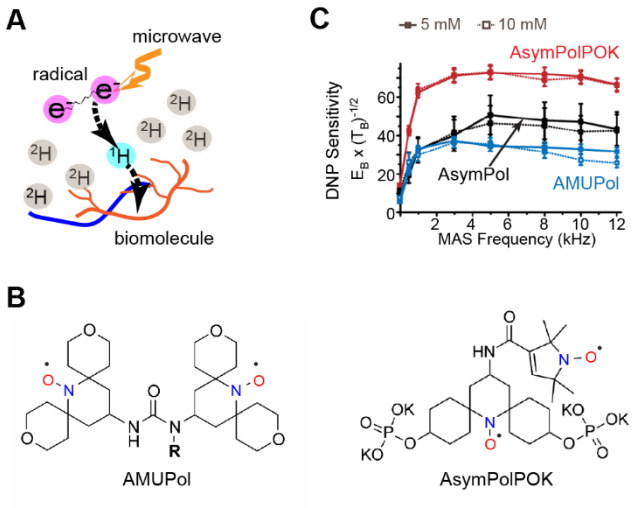

Figure 3.1. **MAS-DNP technique boosts NMR sensitivity.** (**A**) Illustration of the MAS-DNP mechanism. (**B**) Representative structure of two biradicals, AMUPol and AsymPolPOK. (**C**) Enhancement of the sensitivity of spectra collected on ^{13}C-urea at a variety of magic-angle spinning frequencies at 9.4 T and 105 K using three different biradicals, including AMUPol, AsymPolPOK, and AsymPol at two different concentrations (5 and 10 mM). The MAS-DNP sensitivity is quantified as the signal intensity per unit square root of time.

Thanks to all these developments DNP has turned out to be a versatile technique for addressing the key biochemical questions with structural relevance. Some specific applications will be discussed below.

Membrane proteins and protein-ligand binding

Although the DNP-assisted SSNMR has a unique capability of analysis samples without the need of solubilization and crystallization, it is not without a disadvantage in sample preparation. The sensitivity enhancement obtained for membrane protein analysis is only 20 folds owing to the fact that water accessibility is limited and impermeability of commonly used nitroxide radicals. During the year 2016 the usage of direct titration method to mix the radical and the membrane has resulted in a sensitivity enhancement ($\varepsilon_{on/off}$) of 40-100-fold on a 400 MHz/263 GHz DNP instrument [80]. This method has been employed on two ion for example: the influenza A M2 proton channel and an artificial designed protein channel that co-transports Zn^{2+} and H^{+} ions [87]. The gain in sensitivity has been estimated by comparing by comparing DNP spectra with those

collected at high-temperature (243 K) and the value turned out to be 100-160-fold. Justification of this success has been designated to the bimodal partitioning of radicals in phospholipid membranes, with a surface-resided portion and a membrane-inserted fraction, which can be identified the paramagnetic relaxation enhancement (PRE) effects of unpaired electrons on lipid signals.

The perturbation of chemical shift is used to identify ligand binding sites in proteins at ambient temperatures [88, 89]. Unfortunately, this strategy is incompatible under DNP conditions because of large line-broadening. This made way for new strategies to probe the topography of protein surface and binding of cholesterol and carbohydrate-based ligands. During the year 2013, a new method has been developed by our group which relies on differential isotope-labeling (^{13}C on carbohydrate components and ^{15}N, ^{13}C on recombinantly expressed proteins) for the purpose of investigating the binding of a loosening protein expansin to *Arabidopsis* cell walls [73]. Here DNP does the wonderful job of low functional concentration of this protein, followed by spectral editing techniques enables the detection of protein-bound carbohydrates. The inclusion of expansins to the junctions, where the hemicellulose xyloglucan is entrapped between multiple cellulose microfibrils or between several glucan chains of a single microfibril, turned out to be the polymer assemble produced during cell wall elongation.

Hong's group investigated protein-cholesterol binding in lipid bilayers by utilizing ^{13}C-labeled cholesterol from [38]. The cholesterol obtained by genetically engineered strain (RH6829) of *Saccharomyces cerevisiae* which changes the metabolism to produce cholesterol instead of sterol ergosterol has been alternatively ^{13}C-labeled using either 1- or 2-^{13}C glucose (**Fig. 3.2.A**). Thankfully sensitivity enhanced by DNP, two-dimensional (2D) ^{13}C–^{13}C double-quantum filtered (DQF) spectra have resolved several cross peaks corresponding to interactions influenza A virus

M2 protein and the 1-^{13}C cholesterol in lipid bilayers explicitly and it was combined with the previous evidence on helix orientation and binding stoichiometry [39] to demonstrate the way in which the M2 protein utilizes its Ile, Leu and Phe sidechains on an annular binding site of the transmembrane helix to bind cholesterol asymmetrically via methyl-methyl and CH-π interactions (**Fig. 3.2.A**). mechanisms through which M2 proteins interact with membrane components, promote membrane curvatures [90-92], and facilitate membrane scission during virus budding and release [93] has been clearly brought to light by the following results.

In order DNP efficiency and site selectivity of protein or membranes there have been continuous efforts made to covalently link them to mono- or bi-radicals. The spin-labeled phosphocholine (PC) lipids, such as 5-Doxyl PC and 5-Doxyl PC had been used to function as the DNP polarizing agent and as a part of the molecule constating the lipid bilayers [85]. As a result, homogenous polarization has been observed across the lipid bilayers and to a lung surfactant mimetic peptide KL_4 inserted in these membranes. Using similar technique site-directed incorporation of polarizing agents has been displayed on the potassium channel KcsA, the antibiotics gramicidin, and the sensory rhodopsin [94-96].

On the other hand, radicals are paramagnetic species which means the spins in their spatial vicinity thus often experience line broadening and intensity suppression. Hence taking advantage of the fixed distance between the two species, the amount signal quenching, also called paramagnetic bleaching, can be determined in case of direct binding of radical to a protein (**Fig. 3.2.C**). This method have been to study the distance between a combined ligand-radical and the reductase of *E. coli* bacteria [97]. The DNP spectral comparison of ligand strongly bound to protein

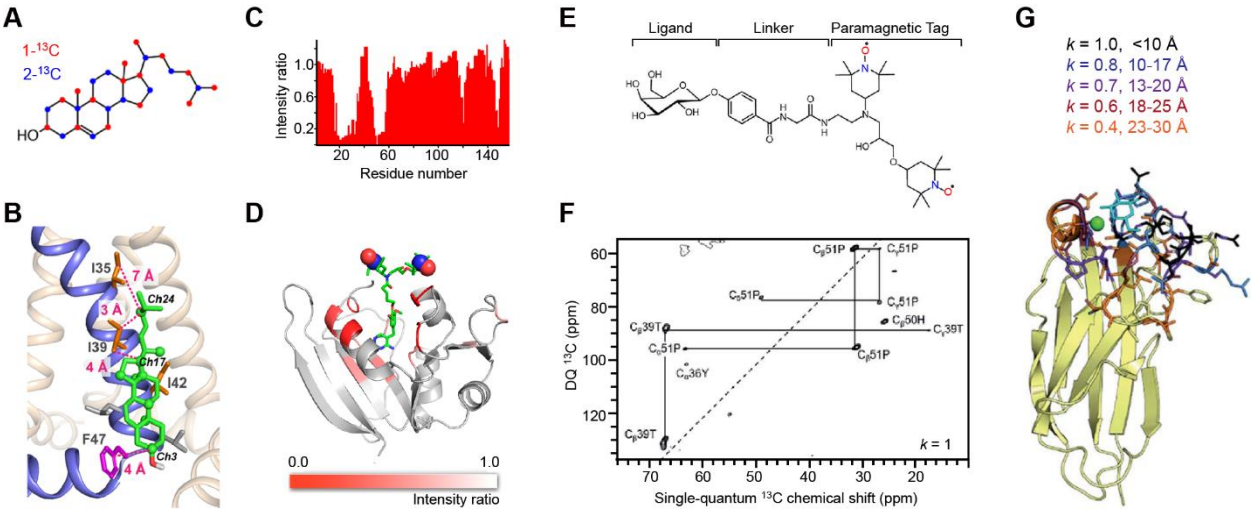

Figure 3.2. **MAS-DNP methods for probing protein-ligand binding.** (**A**) Yeast-based ^{13}C labeling of cholesterol using site-specifically ^{13}C-labeled glucose. The labeled carbon sites on cholesterol are in red and blue for cholesterols produced from 1-^{13}C and 2-^{13}C glucose molecules, respectively. (**B**) A structural model of a cholesterol molecule bound to the influenza M2 proteins. The key Ile and Phe residues, as well as their distances to cholesterol carbons, are shown. (**C**) Signal bleaching quantified in solution ^{1}H-^{15}N HSQC spectra due to the binding of radicals to dihydrofolate reductase. (**D**) A model of *E. coli* dihydrofolate reductase with DNP bleaching information represented by the intensity ratios of ^{13}C-^{13}C DARR spectra collected on two samples containing either bound radicals or exogenous radicals. (**E**) Scheme for incorporating a carbohydrate ligand to a paramagnetic tag for selective DNP. (**F**) Selective DNP ^{13}C–^{13}C INADEQUATE difference spectrum of LecA obtained using k=1: only the tightly bound residues are observed. (**G**) Sideview of LecA. Residues observed using selective DNP are highlighted, with the corresponding k values given.

and the one with the solvent-bearing, exogenous AMUPol as a reference, highlighted the protein surface involved in binding the target (**Fig. 3.2.D**).

Although it is ironic that signal bleaching improves resolution in protein-ligand binding spectra, covalently linked ligand (for example, carbohydrates) with a polarizing agent (a TOTAPOL) through a phenylglycine linker has proven to do just that (**Fig. 3.2.E**) [86]. We also shown similar things can be achieved with the studies of *E. coli* reductase as discussed above, by finding the difference between two spectroscopies in addition to functionalization [98, 99]. One of the spectra is acquired using the paramagnetically tagged sample and it is subtracted from a reference spectrum of a sample that only contains of paramagnetically tagged sample before spectral

subtraction. Thus, making it work like an atomic-resolution microscope with adjustable magnification so that only the tightly bound residues (<10 Å) can be observed in the difference spectrum when *k*=1 is applied, and it up to 30 Å with a decreasing *k* value (**Fig. 3.2.F**). This method has been successfully used to study a galactose-specific lectin LecA and the spectral subtraction provides remarkable resolution, allowing us to unambiguously locate the carbohydrate-binding spots on LecA (**Fig. 3.2.G**). Here we do not need prior knowledge of binding site neither does it have a limitation on the protein size.

Protein structure in cellular fractions or intact cells

In the year 2015, a one-megadalton protein complex, the type IV secretion system core complex (T4SScc) in the cell envelope fractions of *E. coli* had been studied[100]. This shows how huge sensitivity in DNP reduced the dilution limit for the biomolecules in cellular fractions or whole-cells. In the cellular system the result obtained are consistent with the X-ray crystallography results. Likewise, another protocol has been established to study protein folding in cellular lysates that involves both selective labeling producing NMR-active prion proteins and an NMR-silent cellular environment (**Fig. 3.3.A**) [74, 101]. For example the folding of an intrinsically disordered region of the yeast prion protein Sup35 has been determined using it where fibrils are found to be fully restructured and differ from *in-vitro* templated assemblies [74]

The investigation of intact human cells using DNP-NMR, has been a challenge for a long time both because of the lack of suitable radical preparation method and highly demanding experimental condition. There had been three steps protocol developed during 2019 to study

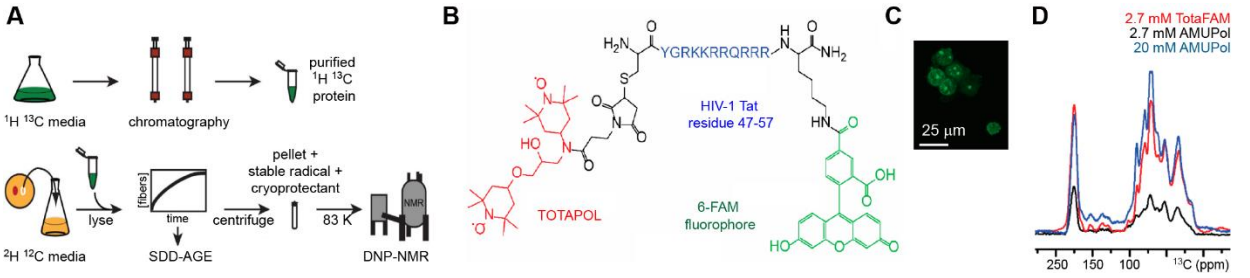

Figure 3.3. **Cellular MAS-DNP of protein structure.** (**A**) Preparation of proteins at endogenous levels for MAS-DNP in biological environments. (**B**) Chemical structure of the trimodal polarizing agent TotaFAM. (**C**) A fluorescent image confirms the cellular uptake of TotaFAM. (**D**) 1D ^{13}C spectra of HEK293F cells below 6 K, using different radicals.

proteins in mammalian cells. These were as follows :isotope labeling the protein of interest, delivery of the protein into cells by electroporation techniques followed by a stimulus to the cells, and introduction of radicals for DNP measurements [102]. Using microscopy techniques to investigate both cell wall integrity and biradical distribution, it was observed that the model protein ubiquitin has been correctly folded after delivery into HeLa cells [102]. Another study done around the same time quantified the chemical reduction effect of nitroxide biradicals in *E. coli* pellets, suspensions and lysates. The redox activity of the nitroxide radical can be suppressed by treating the cell using N-ethylmaleimide. This prevents the redox-active cysteines. This redox activity can be restored by adding potassium ferricyanide, which re-oxidizes the reacted radicals back into their active state[103]. Fluorophore was used to track radicals in the cell alongside a trimodal polarizing agent TotaFAM, which contains a biradical, a targeting cell-penetrating peptide back in 2018 (**Fig. 3.3.B**)[75]. There has been a high sensitivity enhancement of 63-fold using low concentration (2.7 mM) of the radical proving its uptake being very efficient in HEK293F cells (**Fig. 3.3.C**). A very high concentration of around 20 mM is required for commercial radicals to achieve similar

sensitivity enhancement (**Fig. 3.3.D**). Overall, these outstanding achievements have enabled better understanding of the molecular structure, functional mechanisms, and drug inhibition [104] of protein machinery as well as other biomolecules in their cellular context.

Biopolymer packing in fungal and plant cell walls

Plant and microbe cell walls are surrounded by protective armor of cells and they are currently matters of great increase due to potential energy source and the target of antibiotics and antifungal therapies[2, 105]. There have been varieties of organisms studied using SSNMR, including the cell walls of many plants, pathogenic fungi, microalgae, and bacteria for the past ten years [106-112]. Under cryogenic conditions highly rigid and partially crystalline components of cellulose microfibrils in plants and chitin in fungi, have shown greater resolution at cryogenic conditions [32, 73, 113]. This makes carbohydrate-rich cell walls perfect target for DNP investigations. Alongside this, the NMR fingerprints of cell wall polymers are different from those of intracellular and metabolic carbohydrates or other molecules (e.g. proteins and nucleic acids). As a result, cell walls can be spectroscopically distinguished from other cellular components.

During recent times our group have been adept at elucidating the structural organization of cell walls in fungal pathogens, beginning with model fungus *Aspergillus fumigatus* [32] and reaching towards yeasts as well as molds. Around 30-fold of sensitivity enhancement using DNP has enabled us to demonstrate highly polymorphic nature of biomolecules in intact cell walls and efficiently probe their sub-nanometer packing. Although chitin concentration is low (~10% of the dry mass of *A. fumigatus* cell walls), it exists in three major forms as shown by the peak multiplicity of 2D ^{15}N-^{13}C correlation spectra (**Fig. 3.4.A**). The chemical shift belonging to these signals change depending on its sources [114, 115]. The main reason for this surprising level of structural polymorphism is the different possibilities of hydrogen-bonding (through the amide and carbonyl

groups) to form parallel, anti-parallel, and mixed ways of packing in chitin microfibrils [116, 117]. The 2D ^{15}N-^{15}N Proton Assisted Recoupling (PAR) experiment showed mixtures of individual fibrils [118-120]. The mechanical framework of tightly associated chitin and α-1,3-glucans has been identified combining the difference spectroscopy and DNP, which increases both spectral sensitivity and resolution. Further combination with the NMR data collected at room temperature showed that this scaffold resides in a soft matrix of β-glucans and capped by a shell rich in glycoproteins.

DNP has been used to probe physical contacts between multiple polysaccharides and the aromatic polymer lignin (a low concentration polymer), in the secondary cell wall of plant. It was possible to have well-resolved aromatic signals from lignin and determine the polysaccharide composition in the vicinity using dipolar and frequency filters alongside mechanical shutter for precise regulation of microwave on the millisecond timescale [121]. signals from the internal and surface glucan chains in the microfibrils are either missing or weak (**Fig. 3.4.B**) showing that cellulose lacks interactions with lignin in maize stems, which shifts the current paradigm. However, hemicellulose xylan, which primarily relies on its disordered 3-fold conformers (3 residues per helical turn) to bind lignin and use the 2-fold flat-ribbon domains has been found to connect to cellulose microfibrils. The immobility of the aromatic-carbohydrate interface enables understanding of the polymer interactions underlying the nanoscale architecture of this biological assembly and reorganize current thinking related to lignocellulosic biomass. Other than this DNP has also been used to identify the carbohydrate and lignin constituents of poplar and its genetic

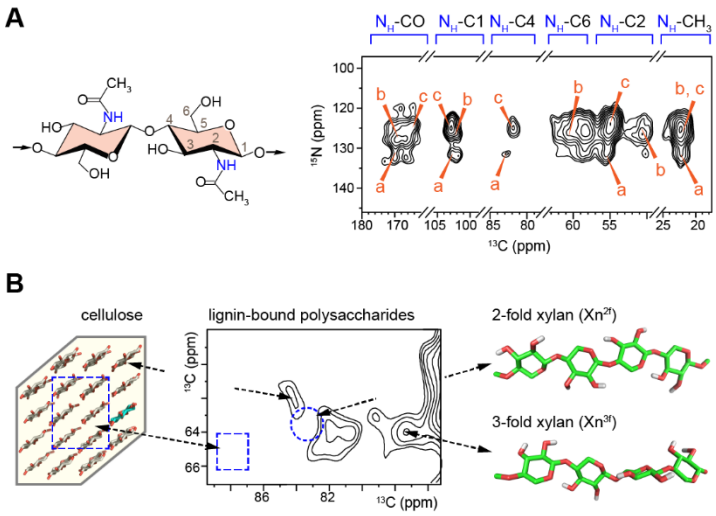

Figure 3.4. **Polysaccharide structure and polymer binding in plant and fungal cell walls.** (**A**) Representative structure and MAS-DNP spectra of chitin in cell walls of intact *A. fumigatus*. Three major types of chitin signals have been resolved (Types a-c). (**B**) The aromatic-edited spectrum of maize stems shows the signals of lignin-bound carbohydrates. Arrows and black dotted lines connect the spectral regions with polysaccharide structures. Dashed line circle and rectangle on the spectrum highlight the missing signals of the carbohydrate components that are far from lignin.

variants after chemical treatments, which will help develop biomass conversion technologies [122, 123].

Apart from the ones mentioned above various other DNP studies has been performed on complicated biological such as the DNA and coat proteins of the filamentous phage Pf1 using intact virus, the supramolecular assembly of HIV capsid, the peptidoglycans in *Bacillus subtilis* bacterial cell walls, the nucleic acids in bones, the post-translational collagen modification in muscle cell extracellular matrix, as well as the surfaces and interfaces of biominerals [12, 76, 124-130]. The ability of DNP should be protracted to characterizing a sample at natural abundance which elements the necessity of isotope-enrichment by using the analytical software that facilitate spectral and structural comparisons [131-134], which has the ability to enhance research in biological area.

Chapter 4. Conclusion

In this current study we have successfully determined structural changes brought about by genetic mutation using a combination of high resolution SSNMR studies and chemical analyses. In addition to this we have also determined some key components responsible for cell wall association as well as glycoprotein linkages via alkaline treatment of the control sample. Fungal cell wall consists of two parts: the inner cell wall and the outer layer encapsulating the inner cell wall. The inner cell wall consists of rigid and hydrophobic cluster of α-1,3-glucan and chitin along with soft and hydrophilic matrix of β-1,3-glucan and this structural framework is well complemented by β-1,3-glucan covalently bonded to chitin. On the other hand, α-1,3-glucan is connected to chitin-β-glucan-GM core via physical interactions. The GM molecule involved in formation of this core is alkaline insoluble whereas the portion of it which lies in the exterior mobile layer of the cell wall alongside protein, GAG and α-1,3-glucan, can be extracted via alkaline treatment. According to dynamics studies, some portion of β-1,3-glucan and α-1,3-glucan are mobile although they are not alkali extractable whereas the rest of it, closely associated with chitin, are alkali extractable. This indicates alkaline extractability being unrelated to actual mobility.

The comparison of parental cell wall with α-1,3-glucan, GAG and GM deficient cell wall showed that the removal of these polysaccharides results in decrease of cell wall thickness. Chitin deficiency causes the most perturbation of the cell wall. The removal of α-1,3-glucan increases β-1,3-glucan content and rigidifies of chitin, making it more hydrophobic. Similarly, in the chitin deficient sample there are major changes occurring with increase in the amount and hydrophobicity of α-1,3-glucan and β-1,3-glucan indicating large extent association of these polymers. Hence roles played by chitin and α-1,3-glucan are unique and cannot be compensated by replacing one with

the other. The removal of GM causes major protein depletion and huge increase of chitin whereas GAG deficiency increases GM content. Analysis of major amino acids constituting protein showed that they generally maintain strong α- helicity and valine is responsible for strong glycoprotein linkages via GM and GAG. These thing demands further investigation possibly by SDS-PAGE. Overall fungi compensate for polysaccharide deficiency by compositional changes in the inner cell wall and the outer layer along with changes in the protein content via complicated biosynthetic pathways. This is in turn changes dynamics and hydration properties as well. The cell wall hydration is maximum when it has a fixed proportion of polysaccharides as seen in the parental cell wall. Further insights into the reasons behind cause and effects of insignificant morphological changes caused by α-1,3-glucan deficiency and severe changes brought to it by chitin deficiency may pave the way for new anti-fungal targets.

The recent advancements on MAS-DNP have successfully eliminated barriers of sensitivity enhancement due to initial depolarization, impermeability of the membrane by the DNP juice and stability of the radical. These made it possible to study functional mechanism, drug binding and change in molecular structure of proteins in their native cellular environment. Likewise, it is now possible to distinguish cell wall from other cellular components in the plant biomass. The arrangement of α-1,3-glucan, chitin and β-1,3-glucan along with the ability of chitin to form allomorph inside the fungal cell wall has been brought to light. Continuous development will increase the dilution limit of this method and make ways for the advent of novel biomaterials.

Appendix A. Supplementary Information of Chapter 2.

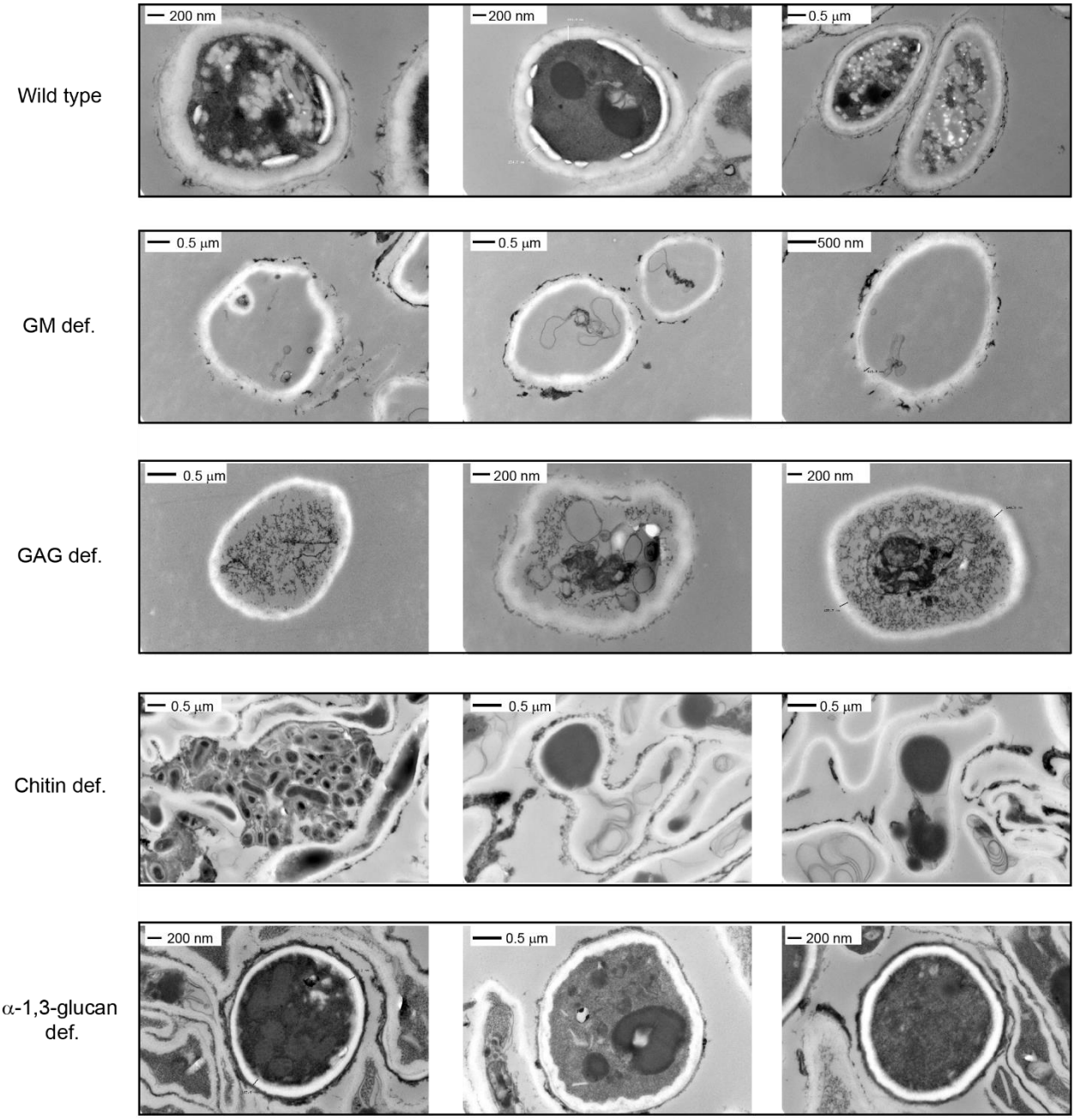

Supplementary Figure A.1. **Transmission electron microscopic images of all the strains.** From top to bottom, representative TEM images are shown for wild-type strain, GM-deficient strain, GAG-deficient, chitin-deficient, and α-1,3-glucan-deficient strain. The length scale is shown for each panel.

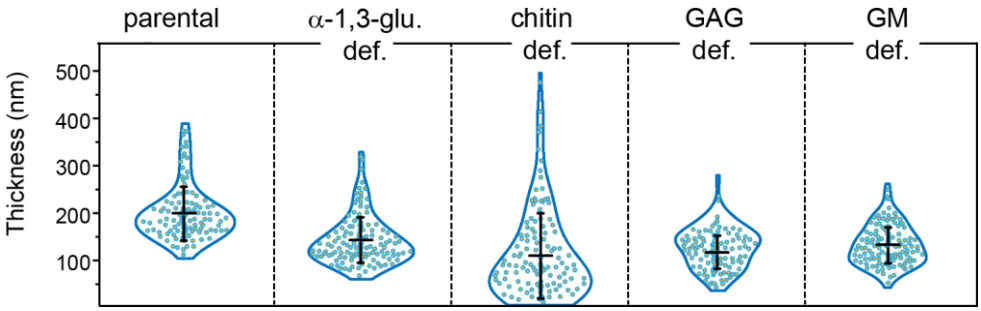

Supplementary Figure A.2. **Distribution of cell wall thickness.** Violin plots showing the distribution of cell wall thickness measured using TEM of parental, chitin-deficient, α-1,3-glucan-deficient, GM-deficient and GAG-deficient cell walls (n=143). *Source*: The entire panel was adapted from reference (54), an open-access article.

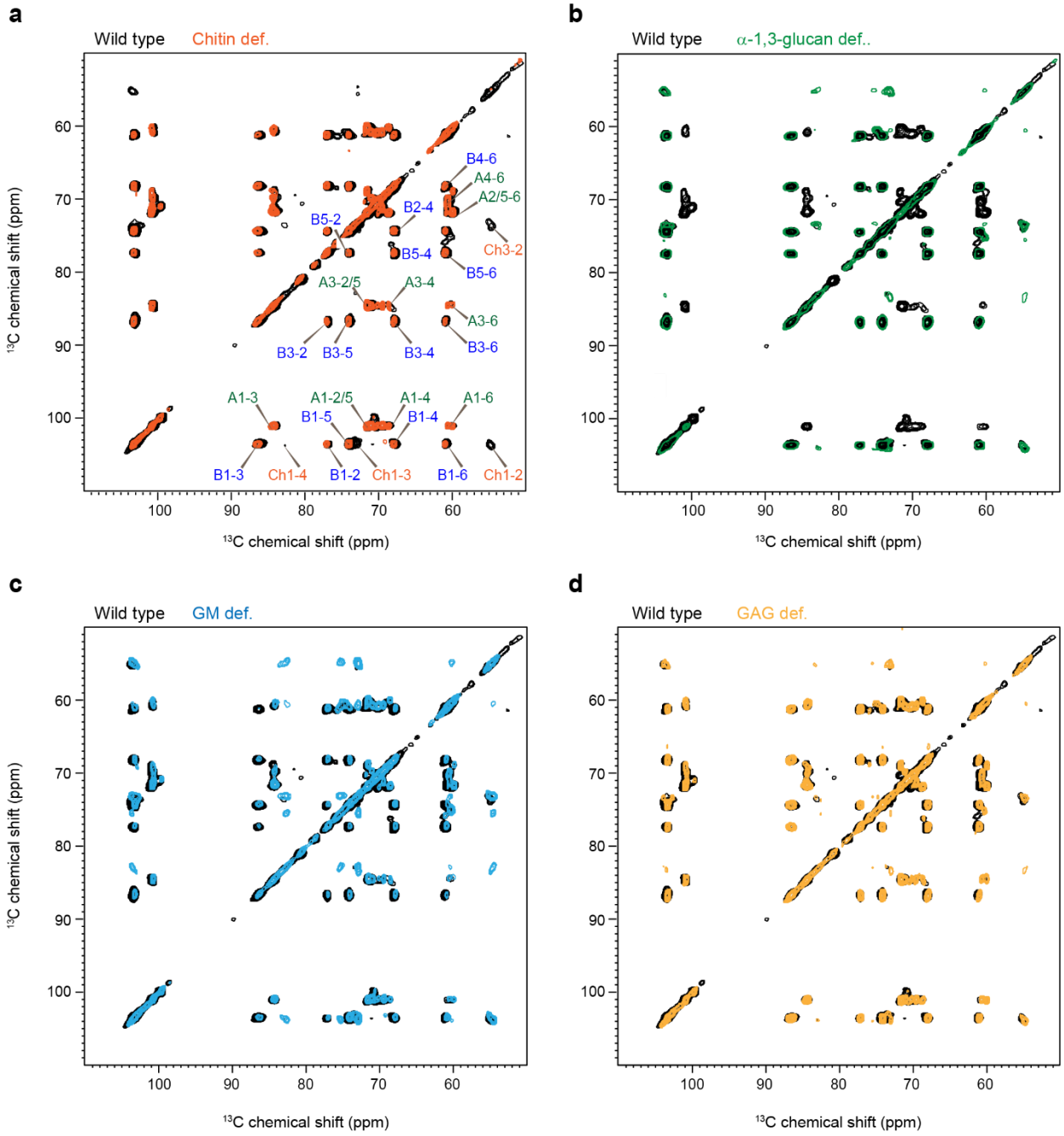

Supplementary Figure A.3. **Comparison of rigid portion of cell walls of *A. fumigatus* and several of its mutants.** Overlapping of wild type (black) spectra with **a** chitin-deficient mutant (orange), **b** α-1,3-glucan-deficient strain (green), showed that chitin and α-1,3-glucan are missing from their respective mutants. While doing the same for **c** galactomannan-deficient mutant (cyan), and **d** galactosaminogalactan-deficient mutant (yellow) showed that chitin increases in GM deficient mutant whereas in GAG deficient mutant there is no significant change. *Source*: The entire panel was adapted from reference (54), an open-access article.

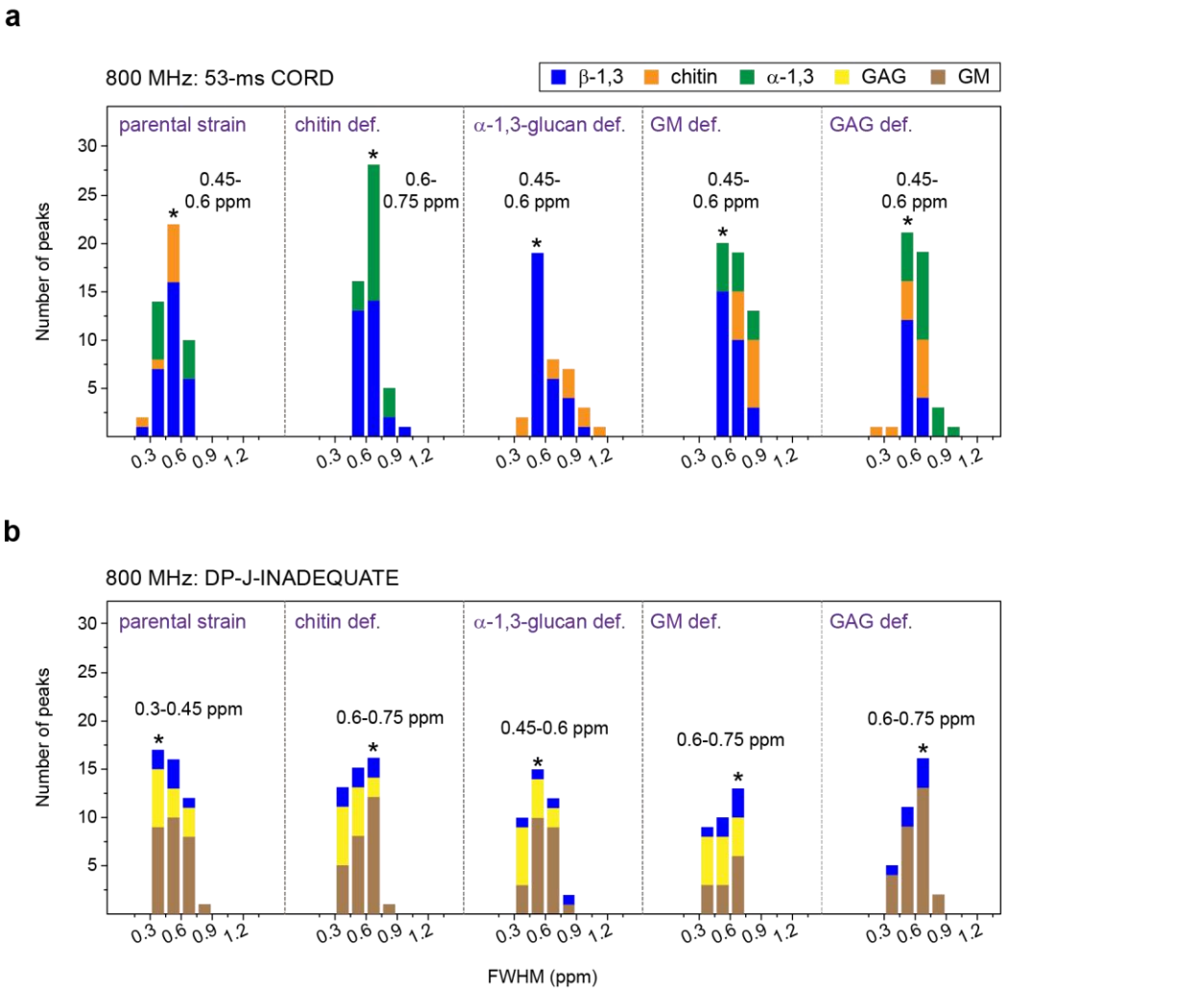

Supplementary Figure A.4. **Linewidth for the peaks included in composition analysis. a** Displays linewidth dispersion of peaks used for analysis of composition of rigid portion. **b** Here we have peaks belonging to spins pairs included in mobile portion composition analysis. *Source*: The entire panel was adapted from reference (54), an open-access article.

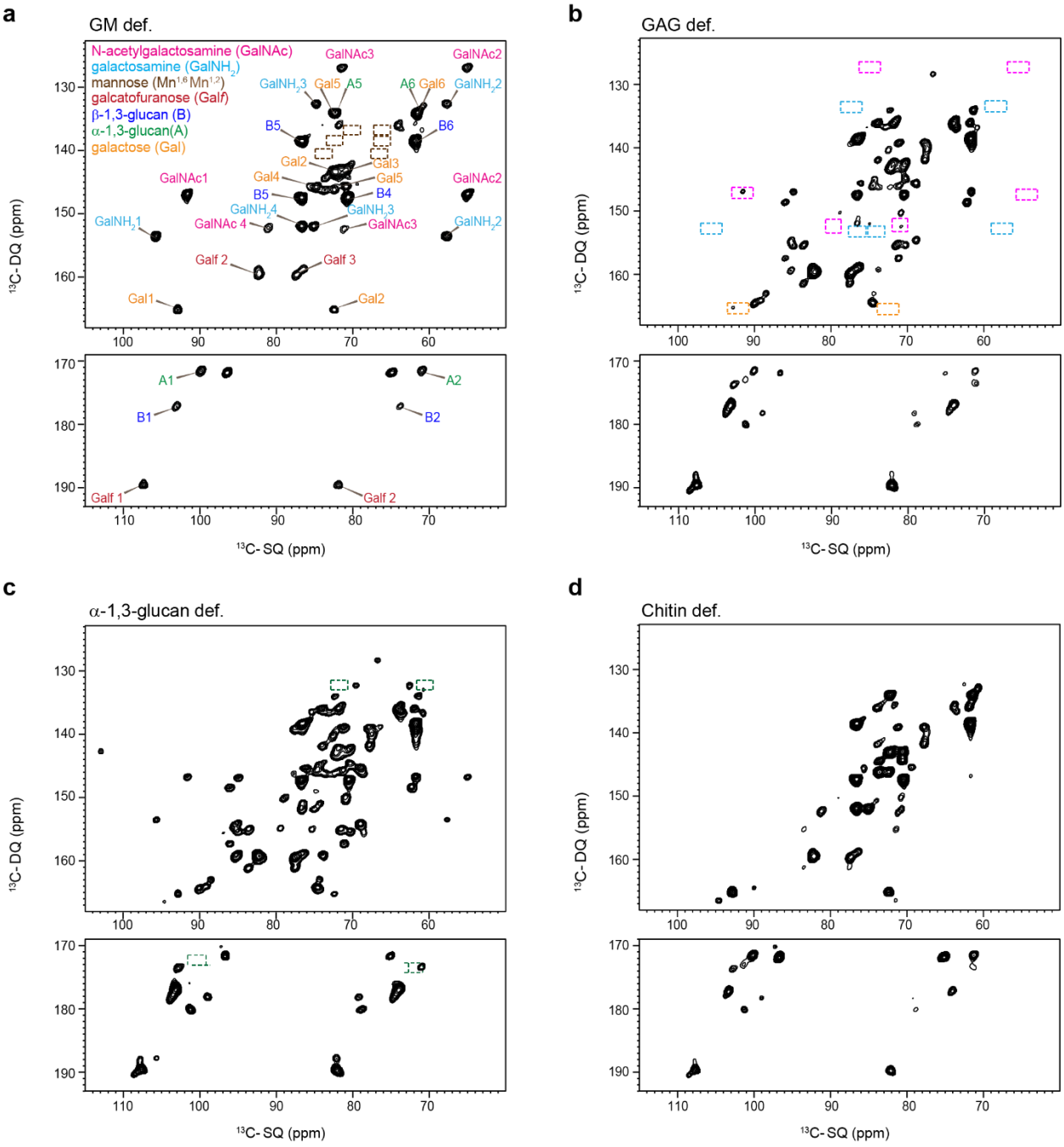

Supplementary Figure A.5. **Mobile region polysaccharides in fungal cell walls.** The missing peaks in 2D ^{13}C DP J-INADEQUATE spectra shown by dashline in **a** GM-deficient mutant, **b** GAG-deficient sample, **c** α-1,3-glucan-dificient strain reflects deficiency of these polysaccharides in the respective mutants and **d** chitin-deficient sample has no missing peaks since chitin does not show up in the mobile region. *Source*: The entire panel was adapted from reference (54), an open-access article.

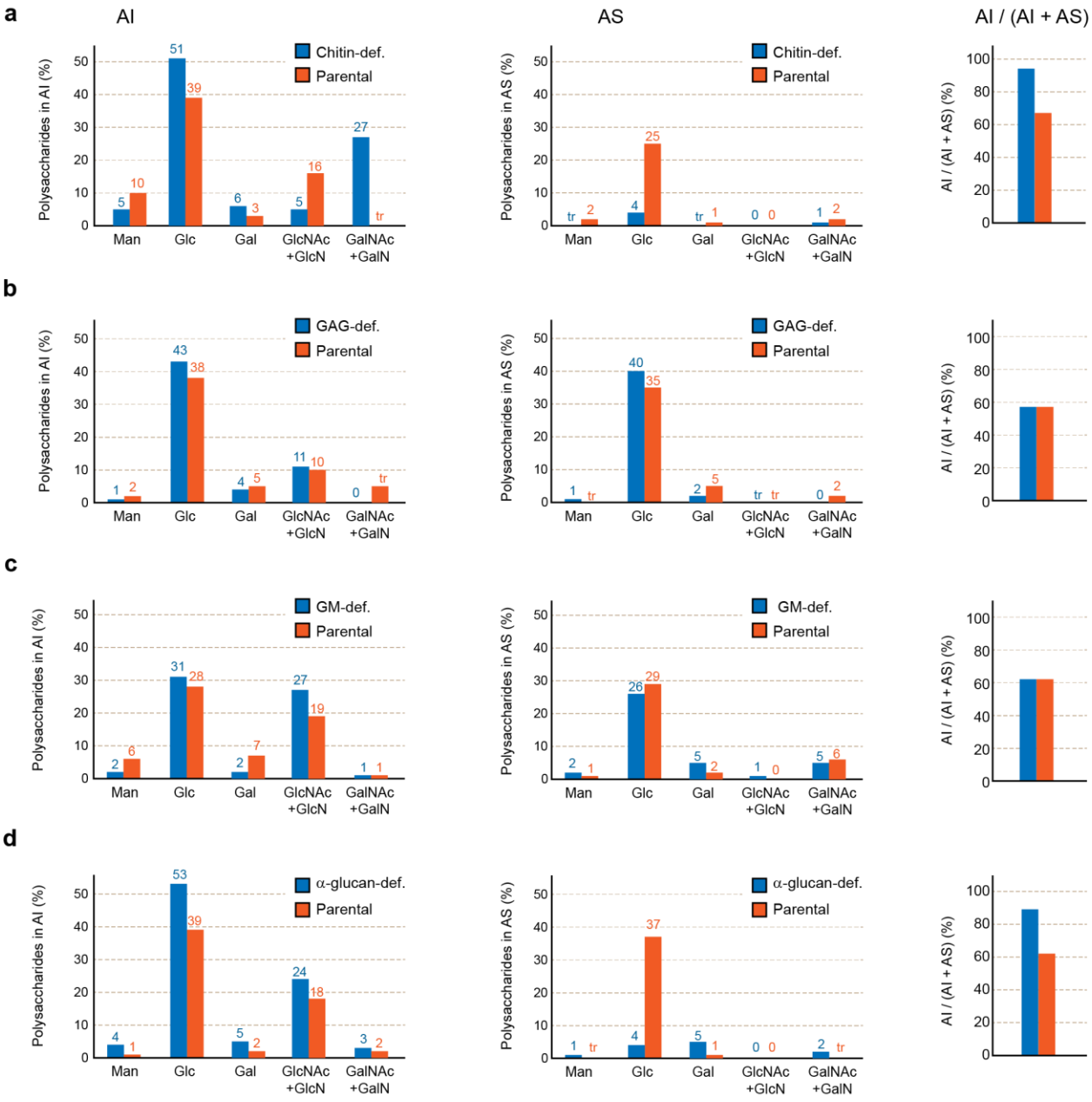

Supplementary Figure A.6. **Hexose and hexosamine composition of *A. fumigatus* obtained via GLC/HPAEC.** The carbohydrate composition of alkali-insoluble (AI, left column) and alkali-soluble (AS, middle column) in **a** chitin-deficient mutant, **b** GAG-deficient mutant, **c**, mannan-deficient mutant, and **d**, α-1,3-glucan deficient mutant is compared with the wild type strain. The panels **a** and **c** show samples grown using Sabouraud media while in panels **b** and **d** Brian media were used for growth. Th right-most panel shows relative proportion of polysaccharides in each sample. *Source*: The entire panel was adapted from reference (54), an open-access article.

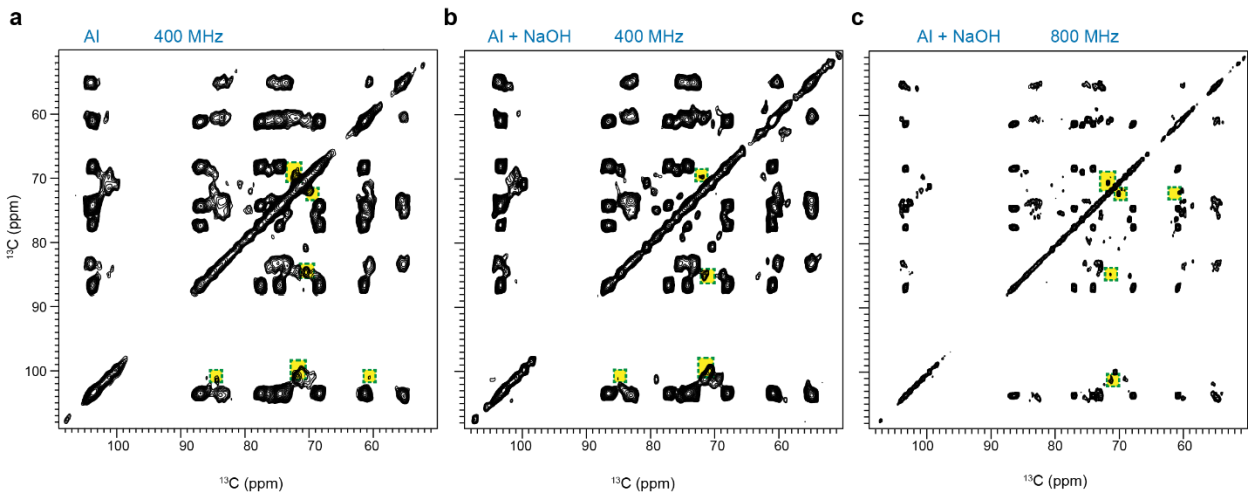

Supplementary Figure A.7. **NaOH treated alkali-insoluble fraction.** ^{13}C-^{13}C 2D CORD spectra of the alkali-insoluble (AI) fraction **a** before a second NaOH treatment, and **b** after a second NaOH at a 400 MHz spectrometer. **c** AI portion treated again with NaOH and measured on an 800 MHz spectrometer, which shows much narrower peaks as benefited from the resolution improvement. Highlighted regions show the α-1,3-glucan signals, which were retained after multiple times of NaOH treatments. *Source*: The entire panel was adapted from reference (54), an open-access article.

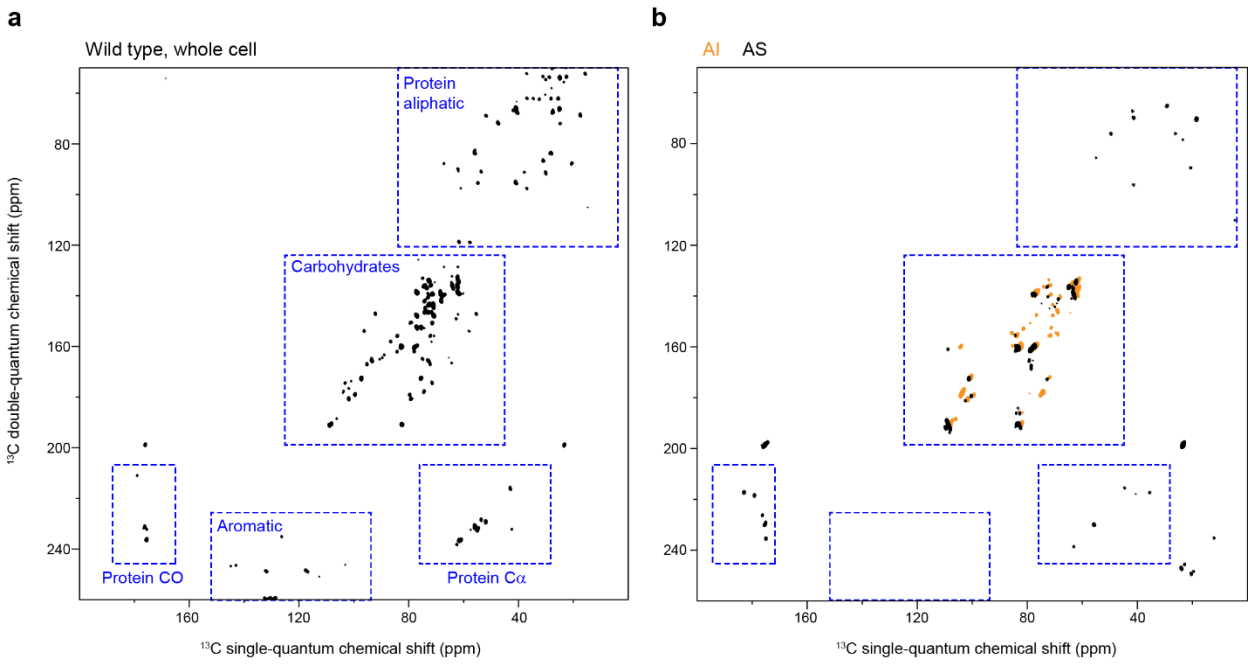

Supplementary Figure A.8. **Comparison of mobile region in whole cell and alkali-treated *A fumigatus*.** **a** Complete ^{13}C DP J-INADEQUATE spectra of wild-type. **b** Overlap of spectra belonging to alkaline-insoluble (AI; yellow) and alkaline-soluble (AS) fractions. Proteins mostly appear in the AS fraction. *Source*: The entire panel was adapted from reference (54), an open-access article.

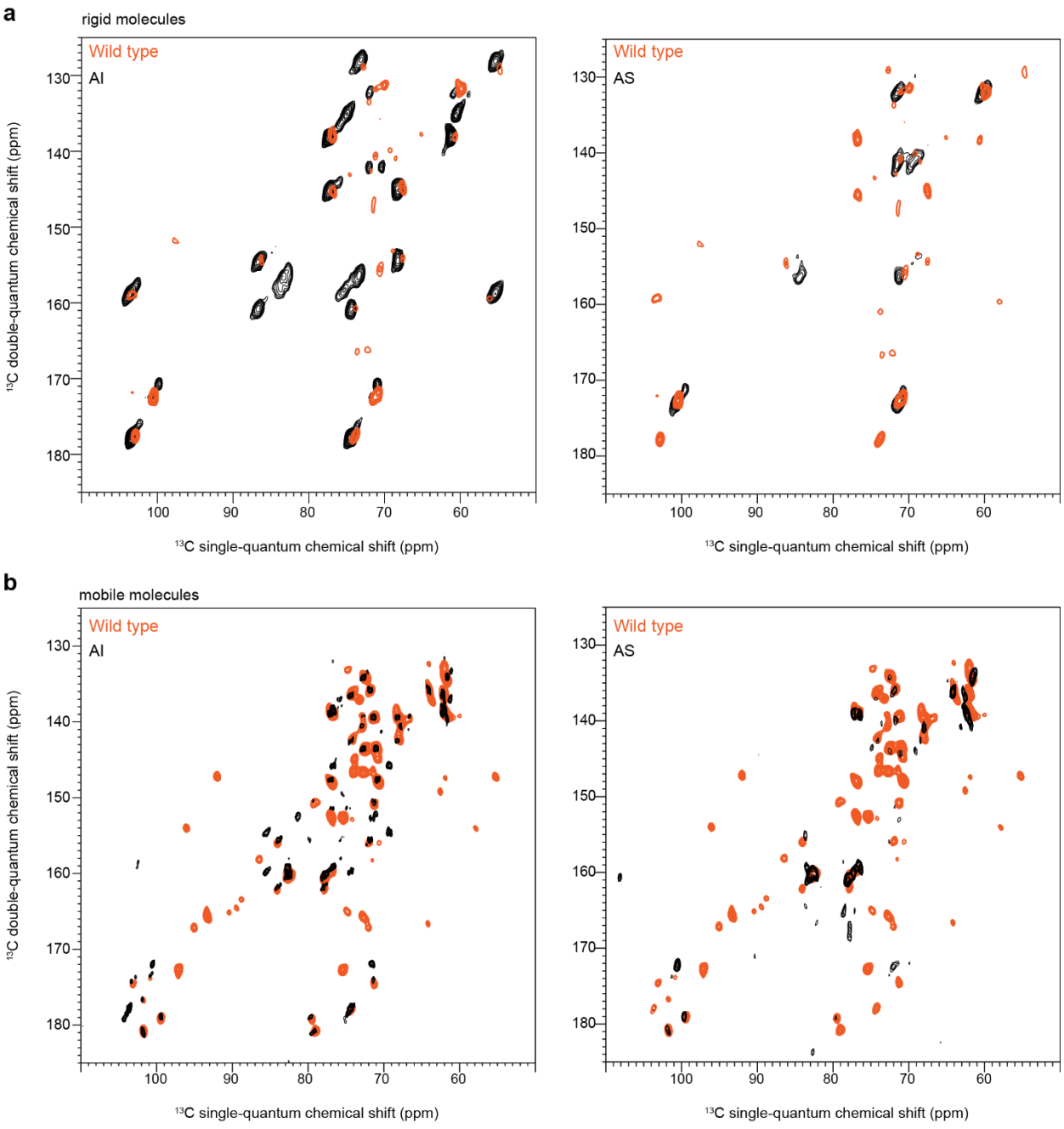

Supplementary Figure A.9. **2D ^{13}C spectra comparison of wild-type cells and alkaline extracts. a** ^{13}C CP INADEQUATE spectra to the wild-type and the alkaline-insoluble (AI) and alkaline-soluble (AS) samples. **b** ^{13}C DP J-INADEQUATE spectra of the samples, these spectrab demonstrates the rigid and mobile molecules respectively in the samples. *Source*: The entire panel was adapted from reference (54), an open-access article.

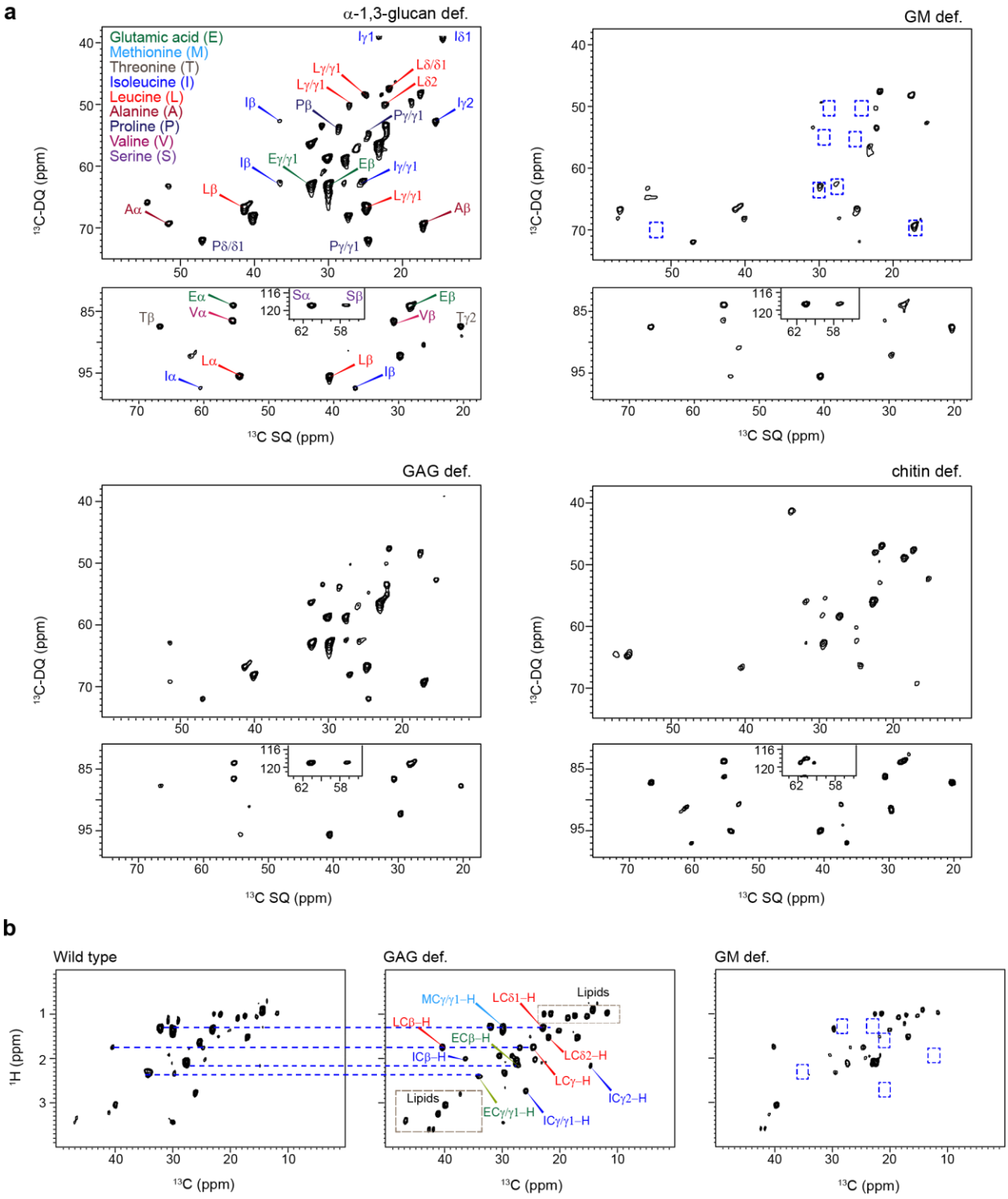

Supplementary Figure A.10. **Mobile-Highly proteins *A. fumigatus.* a** Protein regions of ^{13}C DP J-INADEQUATE spectra where blue boxes missing amino acid signals. **b** 2D ^{1}H-^{13}C INEPT showing highly mobile proteins. Both these spectra confirms beyond doubt that proteins go missing for GM deficient samples. *Source*: The entire panel was adapted from reference (54), an open-access article.

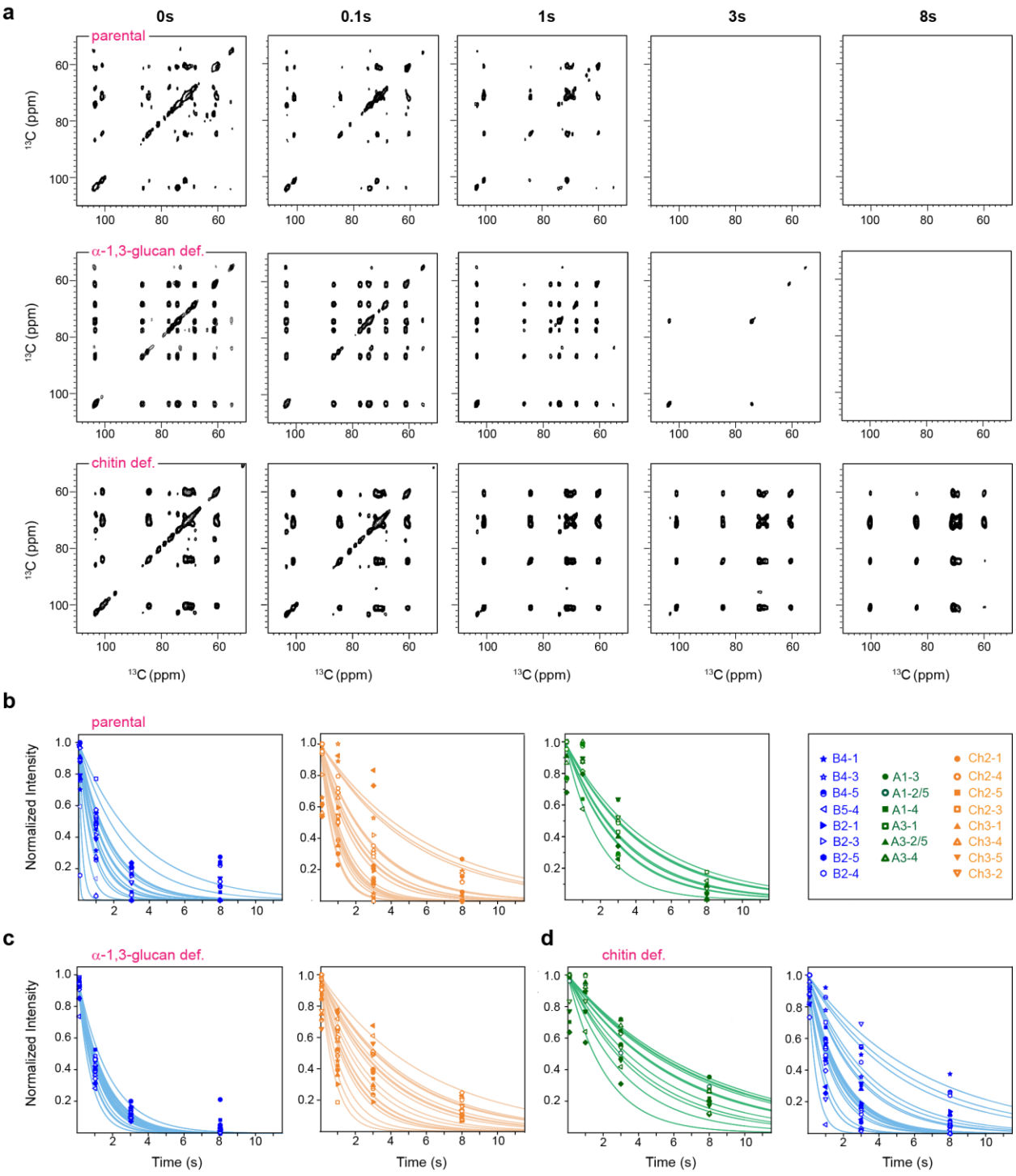

Supplementary Figure A.11. **^{13}C-T_1 relaxation measurements of *A. fumigatus*. a** 2D ^{13}C-^{13}C spectra with a variable z-filter collected on the parental strain (top), □-1,3-glucan-deficient (middle), and chitin-deficient samples (bottom). Within each sample, 5 representative spectra are shown with different z-filter times of 0s, 0.1s, 1 s, 3s, and 8s. ^{13}C-T_1 relaxation curves of polysaccharides of **b** parental strain, **c** a-1,3-glucan deficient strain and **d** chitin-deficient sample were obtained by plotting the normalized intensities as a function of time. Data were collected on a 400 MHz spectrometer and best-fits were obtained using a single exponential equation. *Source*: The entire panel was adapted from reference (54), an open-access article.

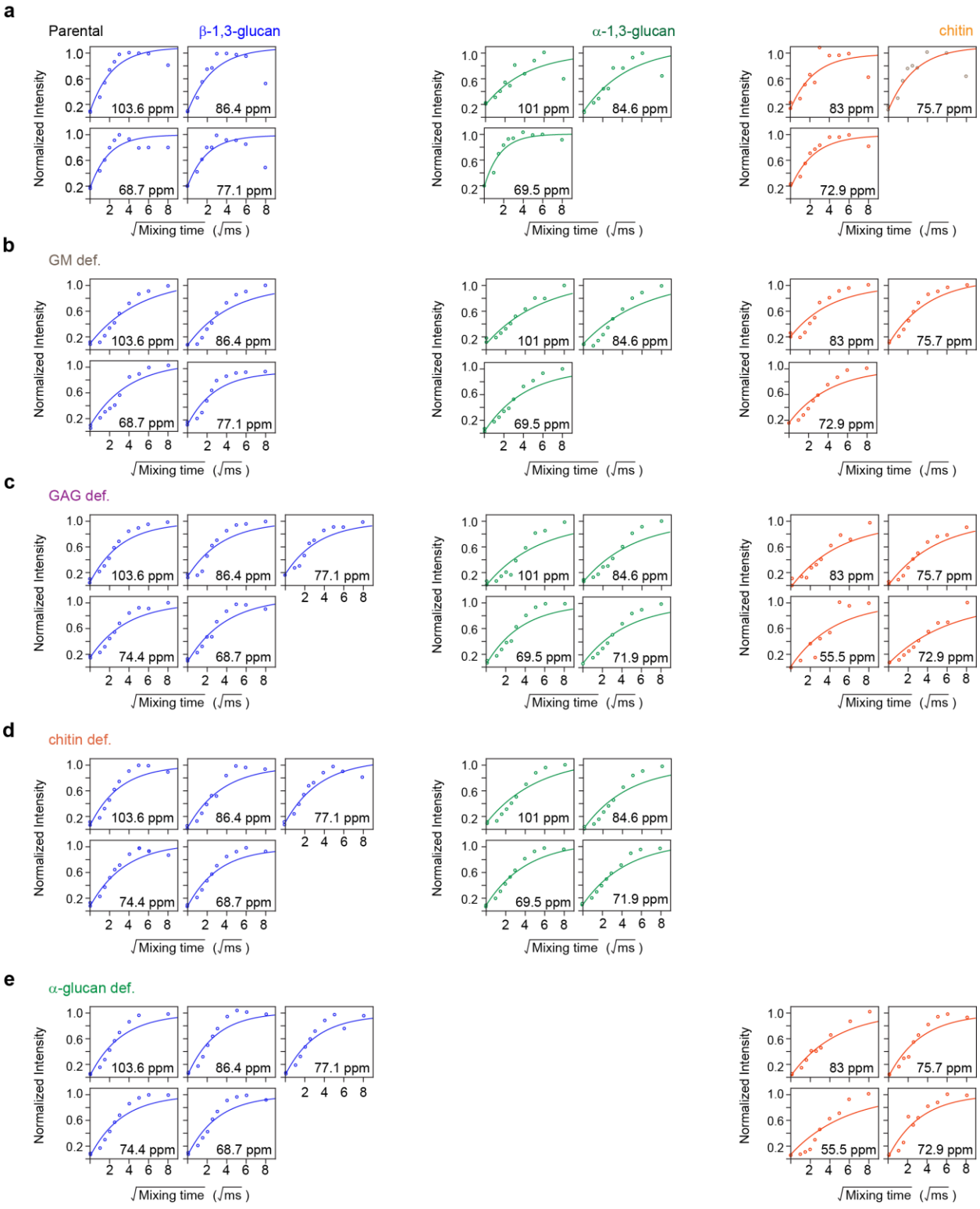

Supplementary Figure A.12. **Water-to-polysaccharide buildup curves.** The data are plotted separately for **a** wild-type sample, **b** GM-deficient mutant, **c** GAG-deficient strain, **d** chitin-deficient sample, and **e** α-1,3-glucan deficient mutant. *Source*: The entire panel was adapted from reference (54), an open-access article.

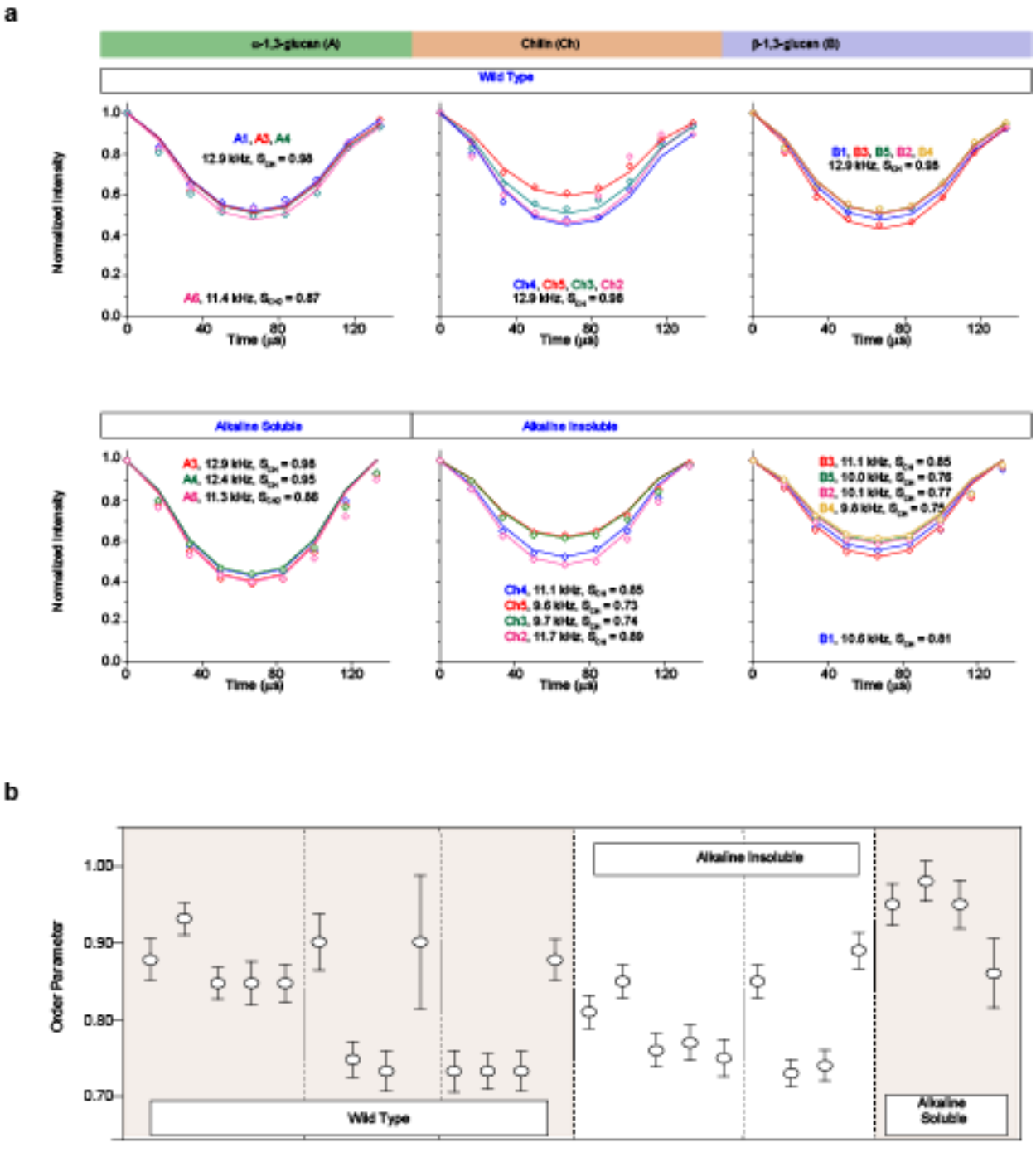

Supplementary figure A.13. **DIPSHIFT data showing how segmental vibration changes after alkaline treatment. a** DIPSHIFT curves for wild type, AI and AS sample. **b** Comparison of order parameter across different samples.

Supplementary Table A.1. **The ^{13}C and ^{13}N chemical shifts of polysaccharides and proteins identified in *A. fumigatus* cell wall**. Superscripts denote different branching of same polysaccharide. Weak signals or minor species are indicated using "w." whereas (/), (-) and Unk: denotes not applicable, unidentified and unknown respectively. *Source*: The entire panel was adapted from reference (54), an open-access article.

Biomolecule	C1	C2	C3	C4	C5	C6	CO	CH_3	N	Experiment	Cell wall portion	References
B	103.6	74.4	86.4	68.7	77.1	61.3	/	/	/	^{13}C -^{13}C PDSD, ^{13}C CP J-INADEQUATE	Rigid	Shim et al. 2007[135] Fairweather et al. 2009[136] Hazime Saitô et al. 1979[137]
B	103.3	74.2	88.3	70.1	77.0	61.2	/	/	/	^{13}C DP J-INADEQUATE	Mobile	Shim et al. 2007[135] Fairweather et al. 2009[136] Hazime Saitô et al. 1979[137]
A	101.0	71.9	84.6	69.5	71.7	60.5	/	/	/	^{13}C -^{13}C PDSD, ^{13}C CP J-INADEQUATE	Rigid	Bhanja et al. 2014[138] Puanglek et al. 2016[139]
Ch	103.6	55.5	72.9	83.0	75.7	60.9	174.8	22.6	123.6	^{13}C -^{13}C PDSD, ^{13}C CP J-INADEQUATE, ^{15}N -^{13}C N(CA)CX-DARR	Rigid	Kono et al. 2004[140] Heux et al. 2000[141] Kameda et al. 2004[115] King et al. 2017[142] Tanner 1990[143]
$Mn^{1,2}$	101.3	78.7	71.2	67.7	73.9	61.7		/		^{13}C DP J-INADEQUATE	Mobile	Latge et al.1994[57]
$Mn^{1,6}$	102.7	70.6	73.2	67.9	73.7	66.1		/		^{13}C DP J-INADEQUATE	Mobile	
Gal*f*	107.5	81.6	77.7	83.5	71.5	63.5		/		^{13}C DP J-INADEQUATE	Mobile	
Gal*p*	93.2	72.2	70.7	73.5	72.5	60.9		/		^{13}C DP J-INADEQUATE	Mobile	Fontaine et al. 2011[64]
GalN	91.7	54.8	71.1	81.1	/	/		/	/	^{13}C DP J-INADEQUATE	Mobile	
GalN'/ GalNAc'	102.5	55.8	71.1	83.6	/	/		/	/	^{13}C DP J-INADEQUATE	Mobile	
GalNAc ("Table cont.d)"	95.7	57.5	75.2	76.9	/	/	175.2	22.7	/	^{13}C DP J-INADEQUATE	Mobile	

Biomolecule	C1	C2	C3	C4	C5	C6	CO	CH_3	N	Experiment	Cell wall portion	References
Leucine	54.9	40.6	24.4	22.7			175.5	21.6	-	^{13}C DP J-INADEQUATE	Mobile	Fritzsching et al. 2013[144]
Leucine	55.1	/	/	22.7			175.6	21.7		^{13}C -^{13}C CORD	Rigid	
Isoleucine	60.7	36.4	25.2	11.9			175.2	15.8	-	^{13}C DP J-INADEQUATE	Mobile	
Alanine	52.1	16.7					176.5			^{13}C DP J-INADEQUATE	Mobile	Fritzsching et al. 2013[144]
Serine "(table cont.d)"	57.3	60.9					174.4			^{13}C DP J-INADEQUATE	Mobile	
Serine	59.2	62.7					174.8			^{13}C -^{13}C CORD	Rigid	
Glutamic acid	55.5	27.7	34.4	/	/	/	175.8	/	-	^{13}C DP J-INADEQUATE	Mobile	
Methionine	53.7	29.4	29.8	/	/	/	176.4	14.2	-	^{13}C DP J-INADEQUATE	Mobile	
Threonine	61.1	66.6	19.9	/	/	/	175.3	/	-	^{13}C DP J-INADEQUATE	Mobile	
Proline	61.3	27.1	24.2	46.8	/	/	174.7	/	-	^{13}C DP J-INADEQUATE	Mobile	
Argenine	55.2	27.9	24.7	25.9	40.9	/	175.8			^{13}C DP J-INADEQUATE	Mobile	
Tyrosine	53.9	34.3	129.3	/	/	115.7	172.9		128.7	^{13}C DP J-INADEQUATE	Mobile	Fritzsching et al. 2013[144]
Tyrosine	55.7	36.4	/	/	/	/	173.2		129.6	^{13}C -^{13}C CORD	Rigid	
Valine	60.8	29.5	17.3	19.5	/	/	173.8	18.6	128.7	^{13}C DP J-INADEQUATE	Mobile	
Valine	60.8	28.6	18.9	19.5			174	/	129	^{13}C -^{13}C CORD	Rigid	

Supplementary Table A.2. **Distribution of cell wall thickness across samples.** Error is the standard deviation of the thickness distribution in each mutant. The average (mean) value is given for each fungal strain. The information related to the *p.* values in unpaired student t-test is described in the method section

Sample Type	Cell	Thickness (nm)	Mean (nm)	*p*.adjust
Wild Type	1	186, 189, 210, 276, 209, 201, 180, 146, 142, 218, 151	206±57	*P*<0.21
	2	196, 159, 237, 188, 177, 184, 209, 163, 270, 199, 202, 197		
	3	287, 113, 185, 199, 165, 212, 158, 171, 148, 183, 154		
	4	201, 175, 242, 192, 163, 157, 172, 152, 169, 130, 145, 160		
	5	148, 192, 223, 168, 210, 175, 124, 195, 167, 225, 130, 130		
	6	199, 180, 160, 350, 278, 204, 213, 190, 202, 341, 171		
	7	188, 163, 145, 169, 166, 203, 174, 160, 128, 142, 142		
	8	170, 164, 167, 157, 175, 168, 163, 147, 161, 144, 163		
	9	245, 222, 163, 182, 165, 178, 180, 208, 197, 201, 193		
	10	242, 221, 199, 187, 244, 182, 208, 217, 205, 186, 201		
	11	340, 373, 374, 320, 309, 326, 366, 261, 296, 317, 296		
	12	211, 242, 202, 190, 199, 221, 200, 236, 227, 199, 204		
	13	312, 226, 283, 298, 319, 324, 259, 286, 329, 201, 250		
Chitin def.	1	94, 108, 109, 172, 137, 182, 166, 130, 125, 125, 115	110±90	*P*<0.04
	2	100, 71, 82, 106, 110, 84, 80, 75, 109, 89, 130		
	3	69, 50, 56, 51, 50, 45, 37, 35, 49, 56, 52		
	4	19, 23, 25, 18, 22, 13, 24, 23, 23, 20, 18		
	5	87, 86, 89, 86, 85, 68, 75, 95, 65, 75, 79		
	6	231, 224, 226, 170, 145, 204, 222, 252, 229, 208, 219		
	7	44, 42, 63, 75, 55, 61, 46, 47, 39, 48,48		
	8	62, 52, 106, 96, 91, 146, 188, 121, 111, 148, 153		
	9	187, 189, 160, 276, 234, 158, 142, 181, 175, 154, 161		
	10	73, 78, 80, 125, 92, 85, 91, 91, 80, 111, 122		
	11	33, 39, 52, 50, 52, 45, 38, 32, 59, 39, 40		
	12	22, 29, 20, 21, 20, 23, 22, 23, 28, 24, 24		
	13	290, 226, 250, 311, 371, 476, 381, 384, 414, 335, 227		
GM def.	1	111, 113, 157, 145, 130, 65, 127, 144, 103, 99, 166	133±38	*P*<0.02
	2	109, 118, 114, 131, 185, 135, 162, 104, 107, 201, 157		
	3	93, 107, 131, 133, 81, 102, 95, 93, 158, 114, 100		
	4	165, 129, 127, 155, 131, 148, 130, 155, 142, 169, 173		
	5	98, 91, 96, 131, 103, 109, 111, 113, 105, 115, 118		
	6	112, 100, 77, 88, 82, 72, 69, 91, 53, 84, 145		
	7	113, 104, 139, 104, 107, 113, 86, 105, 98, 91, 121		
	8	156, 126, 140, 105, 143, 138, 166, 149, 170, 181,195		

“(table cont.d)”

Sample Type	Cell	Thickness (nm)	Mean (nm)	*p*.adjust
	9	134, 96, 101, 104, 100, 93, 85, 93, 88, 87, 86		
	10	135, 137, 121, 121, 123, 112, 150, 118, 133, 144, 111		
	11	189, 180, 189, 138, 211, 143, 187, 191, 231, 230, 179		
	12	146, 146, 250, 161, 156, 192, 129, 177, 170, 178, 134		
	13	200, 147, 195, 187, 173, 144, 189, 235, 161, 163, 178		
GAG def.	1	109, 106, 163, 108, 117, 77, 94, 106, 84, 96, 78	117±35	$P<0.4$
	2	150, 119, 164, 104, 114, 140, 133, 97, 128, 126, 118		
	3	133, 127, 138, 124, 107, 84, 143, 151, 139, 120, 121		
	4	144, 139, 162, 121, 100, 133, 109, 126, 136, 143, 126		
	5	132, 166, 179, 152, 154, 127, 133, 125, 153, 131, 121		
	6	115, 137, 104, 111, 133, 124, 142, 122, 125, 120, 99		
	7	158, 171, 127, 173, 130, 236, 183, 227, 165, 147, 133		
	8	79, 58, 79, 50, 53, 87, 74, 71, 71, 86, 104		
	9	87, 96, 92, 81, 93, 70, 81, 104, 141, 161, 102		
	10	80, 119, 152, 167, 168, 192, 106, 74, 104, 129, 141		
	11	74, 81, 99, 94, 90, 95, 71, 82, 125, 143, 114		
	12	136, 146, 145, 155, 131, 120, 146, 139, 105, 139, 150		
	13	70, 74, 44, 59, 66, 84, 72, 58, 51, 64, 50		
α-1,3-glucan def.	1	224, 235, 253, 293, 319, 243, 242, 313, 252, 198, 230	143±48	$P<0.12$
	2	108, 98, 100, 92, 101, 108, 89, 115, 68, 114, 114		
	3	89, 107, 133, 131, 88, 92, 95, 119, 87, 127, 135		
	4	137, 162, 135, 136, 60, 121, 112, 136, 148, 127, 85		
	5	188, 230, 215, 202, 190, 213, 195, 202, 151, 222, 265		
	6	110, 143, 142, 107, 83, 118, 109, 84, 113, 127		
	7	180, 169, 142, 119, 152, 165, 176, 153, 164, 174		
	8	148, 113, 155, 109, 148, 175, 91, 121, 128, 151, 165		
	9	114, 133, 159, 172, 138, 113, 120, 83, 94, 118, 114		
	10	101, 90, 116, 111, 113, 103, 80, 111, 118, 126, 77		
	11	113, 130, 151, 172, 137, 146, 142, 134, 148, 116, 161		
	12	117, 157, 173, 137, 145, 169, 184, 141, 141, 176, 182		
	13	120, 109, 128, 109, 136, 120, 130, 116, 125, 101, 134		

Supplementary Table A.3. **Variation in rigid polysaccharide composition of *A. fumigatus* with genetic mutation.** UD denotes undetected and error bars are standard errors of cross peak intensities. *Source*: The entire panel was adapted from reference (54), an open-access article.

Wild type			
	β-1,3-glucan	Chitin	α-1,3-glucan
Percentage (mol%)	50±6	8±3	42±7
a-1,3-glucan def.			
	β-1,3-glucan	Chitin	α-1,3-glucan
Percentage (mol%)	95±9	5.3±0.6	UD
Chitin def.			
	β-1,3-glucan	Chitin	α-1,3-glucan
Percentage (mol%)	42±4	UD	58±5
GM def.			
	β-1,3-glucan	Chitin	α-1,3-glucan
Percentage (mol%)	25±2	43±6	32±3
GAG def.			
	β-1,3-glucan	Chitin	α-1,3-glucan
Percentage (mol%)	58±5	5.9±0.8	36±5

The volumes of resolved peaks in 2D ^{13}C-^{13}C CORD spectra belonging to the following:
β-1,3-glucan: the average of C1- C3/C4/C5, C3-C2/C4/C5, C2-C4, C5-C4
α-1,3-glucan: the average of C1-C4, C1-C2/C5
Chitin: the average of C1-C2/ C3/ C4/ C5, C4- C2/C3/C5, C5-C3, C3-C2, C5-C2

Supplementary Table A.4. **Variation in mobile polysaccharide composition of *A. fumigatus* with genetic mutation.** UD denotes undetected and error bars are standard errors of cross peak intensities. *Source*: The entire panel was adapted from reference (54), an open-access article.

Parental

	GM			GAG			β-1,3-glucan	α-1,3-glucan
Percentage (mol%)	Gal*f*	$Mn^{1,2}$	$Mn^{1,6}$	Gal*p*	GalN	GalNAc	4±1	0.83±0.09
	20±2	24±1	5.1±0.3	27±2	13±3	6±1		

a-1,3-glucan def.

	GM			GAG			β-1,3-glucan	α-1,3-glucan
Percentage (mol%)	Gal*f*	$Mn^{1,2}$	$Mn^{1,6}$	Gal*p*	GalN	GalNAc	42±8	UD
	27±2	5±1	4±1	14±1	4.5±0.8	3.0±0.5		

Chitin def.

	GM			GAG			β-1,3-glucan	α-1,3-glucan
Percentage (mol%)	Gal*f*	$Mn^{1,2}$	$Mn^{1,6}$	Gal*p*	GalN	GalNAc	14±3	19±3
	20±3	9±1	7±1	28±4	1.3±0.4	2.0±0.4		

GM def.

	GM			GAG			β-1,3-glucan	α-1,3-glucan
Percentage (mol%)	Gal*f*	$Mn^{1,2}$	$Mn^{1,6}$	Gal*p*	GalN	GalNAc	5.8±0.9	10±1
	7.8±0.9	0.62±0.05	0.97±0.07	33±3	22±4	19±3		

GAG def.

	GM			GAG			β-1,3-glucan	α-1,3-glucan
Percentage (mol%)	Gal*f*	$Mn^{1,2}$	$Mn^{1,6}$	Gal*p*	GalN	GalNAc	42±4	10±1
	33±3	7.0±0.8	8±2	UD	UD	UD		

The volumes of the well-resolved peaks from 2D ^{13}C-^{13}C DP INADEQUATE spectra belonging to the following spin pairs:
mannose ($Mn^{1,6}$): the average of C1,C2,C3,C4
mannose ($Mn^{1,2}$): the average of C1,C2,C3,C4
β-1,5-galactofuranose (Gal*f*): the average of C1,C2,C3,C4
galactopyranose (Gal*p*): the average of C1,C2,C3,C4
galactosamine (GalN): the average of C1,C2,C3,C4
N-acetylgalactosamine (GalNac): the average of C1,C2,C3,C4
α-1,3-glucan: the average of C1,C2,C5 and C6
β-1,3-glucan: the average of C1,C2,C3,C4

Supplementary Table A.5. **The distribution of polysaccharides in AI and AS samples.** The data shows percentage composition of polysaccharides in both the alkali-treated fractions. GAG remains undetected in both fraction, UD denotes undetected. *Source*: The entire panel was adapted from reference (54), an open-access article.

Component	**AI** (mole%)		**AS** (mole%)	
	Rigid	mobile	Rigid	mobile
β-1,3-glucan	49 ± 9	41 ± 15	UD	UD
α-1,3-glucan	14 ± 3	16 ± 4	100 ± 30	14 ± 4
chitin	23 ± 4	13 ± 3	UD	UD
GM	UD	30 ± 10	UD	78 ± 26
Amino acid (valine)	14 ± 3	UD	UD	8 ± 2

Supplementary Table A.6. **Chromatographic analysis of alkaline treated *A fumigatus*.** The percentage composition of polysaccharides in alkali-treated fractions of *A fumigatus* strain harvested in minimal medium, Sabouraud medium and Brian medium. *Source*: The entire panel was adapted from reference (54), an open-access article.

Component	Minimal medium		Sabouraud medium		Brian medium	
	AI	**AS**	**AI**	**AS**	**AI**	**AS**
β-1,3 glucan	47	13	39	1	38	tr
α-1,3 glucan	11	55	2	27	1	36
chitin	22	1	17	0	14	0
GM	7	4	9	2	5	2
GAG	1	9	1	4	4	2

Supplementary Table A.7. The ^{13}C-T_1 relaxation times of polysaccharides in *A. fumigatus* cell walls obtained by fitting data derived from pseudo 3D spectra using single exponential equation $I(t)=e^{-t/T1}$. The standard deviations of the fit parameter are shown as error bars. *Source*: The entire panel was adapted from reference (54), an open-access article.

Sample type		Cross peaks	T_1
Wild type	β-1,3-glucan	B1-3	1.8±0.6
		B1-5	1.4±0.5
		B1-2	1.2±0.2
		B1-4	2.6±0.6
		B3-1	0.5±0.1
		B3-5	1.0±0.4
		B3-2	1.1±0.2
		B5-1	1.3±0.2
		B5-3	4±2
		B5-2	1.2±0.2
		B5-4	0.2±0.1
		B2-1	1.4±0.3
		B2-3	1.4±0.2
		B2-5	1.1±0.03
		B2-4	0.05±0.02
		B4-1	0.7±0.2
		B4-3	1.6±0.2
		B4-5	0.8±0.3
		B4-2	1.7±0.2
	α-1,3-glucan	A1-2/5	4.2±0.9
		A2/5-1	2.9±0.6
		A2/5-4	1.9±0.7
		A3-1	4.3±0.8
		A3-2/5	3.4±0.6
		A4-2/5	2.9±0.9
	Chitin	Ch1-4	5±1
		Ch1-5	2.2±0.4
		Ch1-3	1.2±0.2
		Ch3-5	1.4±0.6
		Ch3-1	1.9±0.1
		Ch5-4	2.9±0.8
		Ch3-5	0.8±0.4
		Ch5-2	2.9±0.2
		Ch4-5	2.8±0.4
		Ch2-1	1.1±0.4
		Ch2-4	2.9±0.4
		Ch2-5	1.2±0.4
		Ch2-3	1.3±0.3
"(table cont.d)"		B1-3	1.4±0.4
		B1-5	1.4±0.1
		B1-2	1.8±0.2

Sample type		Cross peaks	T_1
α-1,3-glucan def,	β-1,3-glucan	B1-4	1.47±0.06
		B3-1	1.18±0.08
		B3-5	1.1±0.1
		B3-2	1.22±0.07
		B5-1	0.88±0.06
		B5-3	1.00±0.07
		B5-2	0.9±0.1
		B5-4	0.7±0.2
		B2-1	1.5±0.1
		B2-3	1.23±0.04
		B2-5	1.14±0.09
		B2-4	1.37±0.09
		B4-1	1.3±0.2
		B4-3	1.2±0.1
		B4-5	1.15±0.07
		B4-2	1.4±0.2
	Chitin	Ch1-4	2.7±0.7
		Ch1-5	3.5±0.9
		Ch1-3	1.8±0.5
		Ch3-5	0.8±0.4
		Ch3-1	1.1±0.4
		Ch5-4	1.3±0.4
		Ch3-5	2.1±0.5
		Ch5-2	2.7±0.7
		Ch4-5	2.05±0.05
		Ch2-1	1.1±0.4
		Ch2-4	2.9±0.4
		Ch2-5	2.0±0.7
		Ch2-3	3.5±0.9
Chitin def,	β-1,3-glucan	B1-3	1.7±0.4
		B1-5	1.5±0.4
		B1-2	2.7±0.5
		B1-4	5.0±0.7
		B3-1	1.8±0.4
		B3-5	1.65±0.04
		B3-2	1.9±0.4
		B5-1	0.8±0.2
		B5-3	1.0±0.2
		B5-2	0.8±0.1
		B5-4	0.46±0.07
		B2-1	1.9±0.7
		B2-3	1.4±0.4
		B2-5	1.6±0.3
		B2-4	3.4±0.9

"(table cont.d)"

Sample type		Cross peaks	T_1
		B4-1	5.5±0.4
		B4-3	1.4±0.4
		B4-5	1.6±0.3
		B4-2	3.4±0.9
	α-1,3-glucan	A1-2/5	5.2±0.7
		A2/5-1	3.9±0.9
		A2/5-4	5.1±0.2
		A3-1	4.0±0.9
		A3-2/5	2.6±0.6
		A4-2/5	3.9±0.8

Supplementary Table A.8. **The water retention times of polysaccharides.** The data obtained for 1D water-edited experiments were fit using exponential growth equation: $I(t) = 1\text{-}ae^{-t/T}$ and error bars represent standard deviations of the fit parameters. The table was adapted from reference (54), an open-access article. *Source*: The entire panel was adapted from reference (54), an open-access article.

Sample type	Assignment	ppm (^{13}C)	Prefactor	$\sqrt{Buildup\ time}$ ($\sqrt{ms}$)
Parental	A1	101.0	0.78	3.8 ± 0.9
	A3	84.6	0.92	3.5 ± 0.6
	A4	69.5	0.80	1.4 ± 0.2
	A2/5	71.9	0.71	1.6 ± 0.2
	B1	103.6	0.88	1.6 ± 0.3
	B2	74.4	0.83	1.6 ± 0.3
	B3	86.4	0.91	1.7 ± 0.5
	B4	68.7	0.81	1.7 ± 0.4
	B5	77.1	0.80	1.8 ± 0.6
	Ch2	55.5	0.84	3.9 ± 0.4
	Ch3	72.9	0.79	2.1 ± 0.3
	Ch4	83.0	0.86	2.2 ± 0.6
	Ch5	75.7	0.88	1.9 ± 0.4
GM def.	A1	101.0	0.88	4.6 ± 0.5
	A3	84.6	0.91	4.8 ± 0.8
	A4	69.5	0.93	3.8 ± 0.4
	A2/5	71.9	0.85	3.9 ± 0.5
	B1	103.6	0.87	4.0 ± 0.5
	B2	74.4	0.88	3.2 ± 0.4
	B3	86.4	0.92	4.0 ± 0.5
	B4	68.7	0.93	3.5 ± 0.4
	B5	77.1	0.83	2.5 ± 0.3
	Ch2	55.5	0.80	5.4 ± 0.9
	Ch3	72.9	0.87	3.9 ± 0.5
	Ch4	83.0	0.75	3.8 ± 0.6
	Ch5	75.7	0.90	3.1 ± 0.3
GAG def.	A1	101.0	0.92	4.8 ± 0.8
	A3	84.6	0.92	4.6 ± 0.7
	A4	69.5	0.89	3.3 ± 0.4
	A2/5	71.9	0.89	4.1 ± 0.5
	B1	103.6	0.94	2.8 ± 0.3
	B2	74.4	0.83	3.4 ± 0.4
	B3	86.4	0.83	3.2 ± 0.5
	B4	68.7	0.85	3.0 ± 0.4
	B5	77.1	0.83	3.1 ± 0.3
	Ch2	55.5	0.90	4.0 ± 0.8

"(table cont.d)"

Sample type	Assignment	ppm (^{13}C)	Prefactor	$\sqrt{Buildup\ time}$ ($\sqrt{ms}$)
	Ch3	72.9	0.93	5.5 ± 0.6
	Ch4	83.0	0.98	4.5 ± 0.5
	Ch5	75.7	0.85	3.9 ± 0.4
Chitin def.	A1	101.0	0.91	4.1 ± 0.6
	A3	84.6	0.94	4.1 ± 0.5
	A4	69.5	0.91	3.1± 0.3
	A2/5	71.9	0.88	3.5 ± 0.4
	B1	103.6	0.88	2.7 ± 0.3
	B2	74.4	0.86	2.6 ± 0.3
	B3	86.4	0.93	3.1 ± 0.4
	B4	68.7	0.92	2.8 ± 0.3
	B5	77.1	0.86	2.5 ± 0.3
α-1,3- glucan def.	B1	103.6	0.93	2.8 ± 0.3
	B2	74.4	0.91	2.9 ± 0.3
	B3	86.4	0.96	2.6 ± 0.3
	B4	68.7	0.90	2.7 ± 0.3
	B5	77.1	0.90	2.8 ± 0.3
	Ch2	55.5	0.96	5.1 ± 0.9
	Ch3	72.9	0.95	3.0 ± 0.4
	Ch4	83.0	0.98	4.3 ± 0.4
	Ch5	75.7	0.93	3.0 ± 0.4

Supplementary Table A.9. Dipolar coupling for polysaccharides. The data were fit using the equation $13.1 \times y = \chi$, where error bars are the standard deviation of the fitting parameters

Sample	Molecule	Peaks	Order Parameter (y)	Dipolar Coupling Constant (χ)
Parental	β-1,3-glucan	B1	0.88±0.03	11.5
		B3	0.93±0.02	12.2
		B5	0.85±0.02	11.1
		B2	0.85±0.03	11.1
		B4	0.85±0.03	11.1
	α-1,3-glucan	A1	0.73±0.03	9.6
		A3	0.73±0.02	9.6
		A4	0.73±0.03	9.6
		A6	0.88±0.03	11.5
	Chitin	Ch4	0.90±0.04	11.8
		Ch5	0.74±0.02	9.8
		Ch3	0.73±0.03	9.6
		Ch2	0.90±0.09	11.8
Alkaline insoluble	β-1,3-glucan	B1	0.81±0.02	10.6
		B3	0.85±0.02	11.1
		B5	0.76±0.02	10.0
		B2	0.77±0.02	10.1
		B4	0.74±0.02	9.8
	Chitin	Ch1	0.85±0.02	11.1
		Ch5	0.73±0.02	9.6
		Ch3	0.74±0.02	9.7
		Ch2	0.89±0.02	11.7
Alkaline soluble	α-1,3-glucan	A1	0.95±0.03	12.5
		A3	0.98±0.03	12.9
		A4	0.95±0.03	12.4
		A6	0.86±0.05	11.3

Appendix B. Permission for reuse

B.1. Copyright permission for Chapter 2.

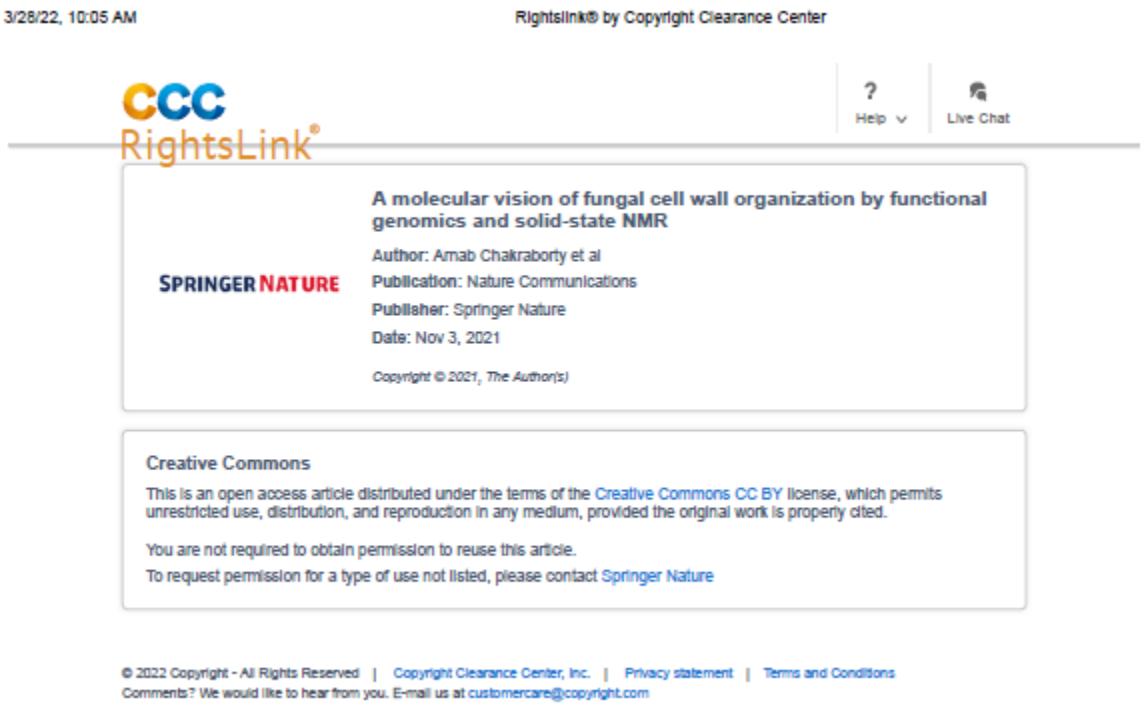

3/28/22, 10:05 AM RightsLink® by Copyright Clearance Center

CCC RightsLink®

Help Live Chat

SPRINGER NATURE

A molecular vision of fungal cell wall organization by functional genomics and solid-state NMR

Author: Arnab Chakraborty et al
Publication: Nature Communications
Publisher: Springer Nature
Date: Nov 3, 2021

Copyright © 2021, The Author(s)

Creative Commons

This is an open access article distributed under the terms of the Creative Commons CC BY license, which permits unrestricted use, distribution, and reproduction in any medium, provided the original work is properly cited.

You are not required to obtain permission to reuse this article.
To request permission for a type of use not listed, please contact Springer Nature

© 2022 Copyright - All Rights Reserved | Copyright Clearance Center, Inc. | Privacy statement | Terms and Conditions
Comments? We would like to hear from you. E-mail us at customercare@copyright.com

B.2. Proof of Principal Authorship of Chapter 3.

Biochemical Society Transactions (2020)
https://doi.org/10.1042/BST20191084

PORTLAND PRESS

Review Article

Biomolecular complex viewed by dynamic nuclear polarization solid-state NMR spectroscopy

Arnab Chakraborty[1], Fabien Deligey[1], Jenny Quach[1], Frederic Mentink-Vigier[2], Ping Wang[3] and Tuo Wang[1]

[1]Department of Chemistry, Louisiana State University, Baton Rouge, LA 70803, U.S.A; [2]National High Magnetic Field Laboratory, Tallahassee, FL 32310, U.S.A; [3]Department of Microbiology, Immunology, and Parasitology, Louisiana State University Health Sciences Center, New Orleans, LA 70112, U.S.A

Correspondence: Tuo Wang (tuowang@lsu.edu)

Solid-state nuclear magnetic resonance (ssNMR) is an indispensable tool for elucidating the structure and dynamics of insoluble and non-crystalline biomolecules. The recent advances in the sensitivity-enhancing technique magic-angle spinning dynamic nuclear polarization (MAS-DNP) have substantially expanded the territory of ssNMR investigations and enabled the detection of polymer interfaces in a cellular environment. This article highlights the emerging MAS-DNP approaches and their applications to the analysis of biomolecular composites and intact cells to determine the folding pathway and ligand binding of proteins, the structural polymorphism of low-populated biopolymers, as well as the physical interactions between carbohydrates, proteins, and lignin. These structural features provide an atomic-level understanding of many cellular processes, promoting the development of better biomaterials and inhibitors. It is anticipated that the capabilities of MAS-DNP in biomolecular and biomaterial research will be further enlarged by the rapid development of instrumentation and methodology.

Introduction

Solid-state nuclear magnetic resonance (ssNMR) spectroscopy has been successfully employed to acquire molecular insights on the structure and dynamics of many biomolecules. Most of these studies are focused on the structural determination of purified or reconstituted biomolecules such as amyloid fibrils, membrane proteins, large protein complex, ion channels and transporters, and nucleic acids [1–9]. Nevertheless, it is technically difficult to conduct high-resolution studies of biomacromolecules in their cellular environments. This limitation is the consequence of two technical issues: the inadequate resolution due to the coexistence of many heterogeneous macromolecules and the unsatisfactory sensitivity due to the low concentration of the molecules of interest. In the past decade, the sensitivity-enhancing dynamic nuclear polarization (DNP) technique has been integrated with specific isotope-labeling techniques and spectral editing approaches that efficiently attenuate spectral congestion. This has made it practicable to study protein folding, biopolymer interactions, and ligand binding using intact viruses and intact cells of bacteria, fungi, plants, and humans [10–15]. This review will summarize the technical feasibility of several emerging approaches and their applications to cellular samples as well as bio-composites. We will also elaborate on how structural restraints can be combined to conceptually comprehend the supramolecular architecture of biological constructs, which could facilitate the development of biopolymer-based materials, bio-sourced energy, and novel therapeutic agents.

Received: 1 March 2020
Revised: 17 April 2020
Accepted: 20 April 2020

Version of Record published:
7 May 2020

MAS-DNP sensitivity enhancement enables new research avenues

NMR is a low-sensitivity technique whose signal-to-noise ratios greatly depend on the gyromagnetic ratio of spins. The cutting-edge technique MAS-DNP takes advantage of the several orders of magnitude higher gyromagnetic ratio of electrons over NMR-active nuclei, such as ^{13}C or ^{1}H, to boost NMR

© 2020 The Author(s). Published by Portland Press Limited on behalf of the Biochemical Society

B.3. Copyright Permission for Appendix A.

3/28/22, 10:05 AM RightsLink® by Copyright Clearance Center

CCC RightsLink®

Help Live Chat

SPRINGER NATURE

A molecular vision of fungal cell wall organization by functional genomics and solid-state NMR

Author: Arnab Chakraborty et al
Publication: Nature Communications
Publisher: Springer Nature
Date: Nov 3, 2021

Copyright © 2021, The Author(s)

Creative Commons

This is an open access article distributed under the terms of the Creative Commons CC BY license, which permits unrestricted use, distribution, and reproduction in any medium, provided the original work is properly cited.

You are not required to obtain permission to reuse this article.

To request permission for a type of use not listed, please contact Springer Nature

© 2022 Copyright - All Rights Reserved | Copyright Clearance Center, Inc. | Privacy statement | Terms and Conditions
Comments? We would like to hear from you. E-mail us at customercare@copyright.com

References:

1 Gamaletsou, M. N., et al. (2014). "Aspergillus osteomyelitis: epidemiology, clinical manifestations, management, and outcome." J Infect **68**(5): 478-493.

2 Brown, G. D., et al. (2012). "Hidden Killers: Human Fungal Infections." Sci. Transl. Med. **4**(165).

3 Jorgensen, K. J., et al. (2014). "Voriconazole versus amphotericin B or fluconazole in cancer patients with neutropenia." Cochrane Database Syst Rev(2): CD004707.

4 Hedayati, M. T., et al. (2007). "Aspergillus flavus: human pathogen, allergen and mycotoxin producer." Microbiology (Reading) **153**(Pt 6): 1677-1692.

5 Walsh, T. J., et al. (1999). "Liposomal amphotericin B for empirical therapy in patients with persistent fever and neutropenia. National Institute of Allergy and Infectious Diseases Mycoses Study Group." N Engl J Med **340**(10): 764-771.

6 Soler, S., et al. (2011). "A comparison of restriction fragment length polymorphism, tetra primer amplification refractory mutation system PCR and unlabeled probe melting analysis for LTA+252 C>T SNP genotyping." Clin Chim Acta **412**(5-6): 430-434.

7 Andriole, V. T. (1993). "Infections with Aspergillus Species." Clin. Infect. Dis. **17**: S481-S486.

8 Bernard, M. and J. P. Latge (2001). "Aspergillus fumigatus cell wall: composition and biosynthesis." Med Mycol **39 Suppl 1**: 9-17.

9 Bulawa, C. E., et al. (1995). "Attenuated virulence of chitin-deficient mutants of Candida albicans." Proc Natl Acad Sci U S A **92**(23): 10570-10574.

10 Sanz, M., et al. (2005). "Candida albicans strains deficient in CHS7, a key regulator of chitin synthase III, exhibit morphogenetic alterations and attenuated virulence." Microbiology (Reading) **151**(Pt 8): 2623-2636.

11 Smith-Moritz, A. M., et al. (2015). "Structural characterization of a mixed-linkage glucan deficient mutant reveals alteration in cellulose microfibril orientation in rice coleoptile mesophyll cell walls." Front Plant Sci **6**: 628.

12 Sergeyev, I. V., et al. (2011). "Chemical Shifts for the Unusual DNA Structure in Pf1 Bacteriophage from Dynamic-Nuclear-Polarization-Enhanced Solid-State NMR Spectroscopy." J. Am. Chem. Soc. **133**(50): 20208-20217.

13 Pilsyk, S., et al. (2018). "Molecular characterization of central cytoplasmic loop in Aspergillus nidulans AstA transporter." Acta Biochim Pol **65**(4): 545-554.

14 Le, T., et al. (2017). "A Trial of Itraconazole or Amphotericin B for HIV-Associated Talaromycosis." N Engl J Med **376**(24): 2329-2340.

15 Ghannoum, M. A. and L. B. Rice (1999). "Antifungal agents: mode of action, mechanisms of resistance, and correlation of these mechanisms with bacterial resistance." Clin Microbiol Rev **12**(4): 501-517.

16 Lin, S. J., et al. (2001). "Aspergillosis case-fatality rate: systematic review of the literature." Clin Infect Dis **32**(3): 358-366.

17 Marco, F., et al. (1998). "Antifungal activity of a new triazole, voriconazole (UK-109,496), compared with three other antifungal agents tested against clinical isolates of filamentous fungi." Med Mycol **36**(6): 433-436.

18 Odds, F. C., et al. (2003). "Antifungal agents: mechanisms of action." Trends Microbiol **11**(6): 272-279.

19 Perlin, D. S. (2011). "Current perspectives on echinocandin class drugs." Future Microbiol **6**(4): 441-457.

20 Lipke, P. N. and R. Ovalle (1998). "Cell wall architecture in yeast: new structure and new challenges." J Bacteriol **180**(15): 3735-3740.

21 Bowman, J. C., et al. (2002). "The antifungal echinocandin caspofungin acetate kills growing cells of Aspergillus fumigatus in vitro." Antimicrob Agents Chemother **46**(9): 3001-3012.

22 Kollar, R., et al. (1997). "Architecture of the yeast cell wall. Beta(1-->6)-glucan interconnects mannoprotein, beta(1-->)3-glucan, and chitin." J Biol Chem **272**(28): 17762-17775.

23 Breinig, F., et al. (2004). "Yeast Kre1p is GPI-anchored and involved in both cell wall assembly and architecture." Microbiology (Reading) **150**(Pt 10): 3209-3218.

24 Henry, C., et al. (2019). "Two KTR Mannosyltransferases Are Responsible for the Biosynthesis of Cell Wall Mannans and Control Polarized Growth in Aspergillus fumigatus." mBio **10**(1).

25 Dague, E., et al. (2010). "An atomic force microscopy analysis of yeast mutants defective in cell wall architecture." Yeast **27**(8): 673-684.

26 Kollar, R., et al. (1997). "Architecture of the yeast cell wall - beta(1->6)-glucan interconnects mannoprotein, beta(1-3)-glucan, and chitin." J. Biol. Chem. **272**(28): 17762-17775.

27 Feldmesser, M., et al. (2000). "The effect of the echinocandin analogue caspofungin on cell wall glucan synthesis by Cryptococcus neoformans." J Infect Dis **182**(6): 1791-1795.

28 Latge, J. P. (2007). "The cell wall: a carbohydrate armour for the fungal cell." Molecular Microbiology **66**(2): 279-290.

29 Opella, S. J., et al. (1987). "Protein structure by solid-state NMR spectroscopy." Q Rev Biophys **19**(1-2): 7-49.

30 Smith, S. O., et al. (1989). "Structure and protein environment of the retinal chromophore in light- and dark-adapted bacteriorhodopsin studied by solid-state NMR." Biochemistry **28**(22): 8897-8904.

31 Tang, M., et al. (2011). "High-resolution membrane protein structure by joint calculations with solid-state NMR and X-ray experimental data." J Biomol NMR **51**(3): 227-233.

32 Kang, X., et al. (2018). "Molecular architecture of fungal cell walls revealed by solid-state NMR." Nat. Commun. **9**: 2747.

33 Muszkieta, L., et al. (2014). "Deciphering the role of the chitin synthase families 1 and 2 in the in vivo and in vitro growth of Aspergillus fumigatus by multiple gene targeting deletion." Cell Microbiol. **16**(12): 1784-1805.

34 Henry, C., et al. (2012). "alpha1,3 glucans are dispensable in Aspergillus fumigatus." Eukaryot. Cell **11**(1): 26-29.

35 Briard, B., et al. (2016). "Galactosaminogalactan of Aspergillus fumigatus, a bioactive fungal polymer." Mycologia **108**(3).

36 Zhao, W., et al. (2021). "Solid-state NMR of unlabeled plant cell walls: high-resolution structural analysis without isotopic enrichment." Biotechnol Biofuels **14**(1): 14.

37 Hediger, S., et al. (2018). "MAS-DNP Enhancements: Hyperpolarization, Depolarization, and Absolute Sensitivity." eMagRes **7**(4): 105-116.

38 Elkins, M. R., et al. (2018). "Determining Cholesterol Binding to Membrane Proteins by Cholesterol ^{13}C Labeling in Yeast and Dynamic Nuclear Polarization NMR." J. Am. Chem. Soc. **140**(45): 15437-15449.

39 Elkins, M. R., et al. (2017). "Cholesterol-binding site of the influenza M2 protein in lipid bilayers from solid-state NMR." Proc. Natl. Acad. Sci. USA **114**(49): 12946-12951.

40 da Silva Ferreira, M. E., et al. (2006). "The akuBKU80 mutant deficient for nonhomologous end joining is a powerful tool for analyzing pathogenicity in Aspergillus fumigatus." Eukaryot. Cell **5**: 207-211.

41 Henry, C., et al. (2019). "Two KTR Mannosyltransferases Are Responsible for the Biosynthesis of Cell Wall Mannans and Control Polarized Growth in Aspergillus fumigatus." mBio **10**(1).

42 Briard, B., et al. (2020). "Galactosaminogalactan activates the inflammasome to provide host protection." Nature **588**: 688-692.

43 Jimenez-Ortigosa, C., et al. (2012). "Chitin synthases with a myosin motor-like domain control the resistance of Aspergillus fumigatus to echinocandins." Antimicrob. Agents Chemother. **56**: 6121-6131.

44 Rienstra, C. M., et al. (2002). "De novo determination of peptide structure with solid-state magic-angle spinning NMR spectroscopy." Proc. Natl. Acad. Sci. USA **99**(16): 10260-10265.

45 Hou, G., et al. (2013). "Broadband homonuclear correlation spectroscopy driven by combined R2(n)(v) sequences under fast magic angle spinning for NMR structural analysis of organic and biological solids." J. Magn. Reson. **232**: 18-30.

46 Lu, X., et al. (2015). "Combined zero-quantum and spin-diffusion mixing for efficient homonuclear correlation spectroscopy under fast MAS: broadband recoupling and detection of long-range correlations." J. Biomol. NMR **61**(1): 7-20.

47 Lesage, A., et al. (1997). "Determination of through-bond carbon-carbon connectivities in solid-state NMR using the INADEQUATE experiment." J. Am. Chem. Soc. **119**(33): 7867-7868.

48 Cadars, S., et al. (2007). "The refocused INADEQUATE MAS NMR experiment in multiple spin-systems: Interpreting observed correlation peaks and optimising lineshapes." J. Magn. Reson. **188**(1): 24-34.

49 Baldus, M., et al. (1998). "Cross polarization in the tilted frame: assignment and spectral simplification in heteronuclear spin systems." Mol. Phys. **95**(6): 1197-1207.

50 Hohwy, M., et al. (1999). "Fivefold symmetric homonuclear dipolar recoupling in rotating solids: Application to double quantum spectroscopy." J. Chem. Phys. **110**(16): 7983-7992.

51 Bennett, A. E., et al. (1998). "Homonuclear radio frequency-driven recoupling in rotating solids." J. Chem. Phys. **108**(22): 9463-9479.

52 Kang, X., et al. (2020). "CCMRD: A Solid-State NMR Database for Complex Carbohydrates." J. Biomol. NMR **74**: 239-250.

53 Poulhazan, A., et al. (2021). "Identification and Quantification of Glycans in Whole Cells: Architecture of Microalgal Polysaccharides Described by Solid-State Nuclear Magnetic Resonance." Journal of the American Chemical Society **143**(46): 19374-19388.

54 Chakraborty, A., et al. (2021). "A molecular vision of fungal cell wall organization by functional genomics and solid-state NMR." Nat Commun **12**(1): 6346.

55 Munowitz, M. G., et al. (1981). "Two-Dimensional Rotational Spin-Echo Nuclear Magnetic-Resonance in Solids - Correlation of Chemical-Shift and Dipolar Interactions." J. Am. Chem. Soc. **103**(10): 2529-2533.

56 Speth, C., et al. (2019). "Galactosaminogalactan (GAG) and its multiple roles in Aspergillus pathogenesis." Virulence **10**(1): 976-983.

57 Latgé, J. P., et al. (1994). "Chemical and Immunological Characterization of the Extracellular Galactomannan of Asperillus fumigatus." Infect. Immun. **62**(12): 5424-5433.

58 Fang, W., et al. (2019). "Mechanisms of redundancy and specificity of the Aspergillus fumigatus Crh transglycosylases." Nat. Commun. **10**: 1669.

59 Valsecchi, I., et al. (2017). "Role of Hydrophobins in Aspergillus fumigatus. ." J Fungi **4**(1).

60 de Dios, A. C., et al. (1993). "Secondary and tertiary structural effects on protein NMR chemical shifts: an ab initio approach." Science **260**: 1491-1496.

61 Wang, T., et al. (2017). "Water Distribution, Dynamics, and Interactions with Alzheimer's beta-Amyloid Fibrils Investigated by Solid-State NMR." J. Am. Chem. Soc. **139**(17): 6242-6252.

62 White, P. B., et al. (2014). "Water-polysaccharide interactions in the primary cell wall of *Arabidopsis thaliana* from polarization transfer solid-state NMR." J. Am. Chem. Soc. **136**(29): 10399-10409.

63 PASAMONTES, L., et al. "Gene Cloning, Purification, and Characterization of a Heat-Stable Phytase from the Fungus Aspergillus fumigatus." American Society for Microbiology **63**(5): 1696–1700.

64 Fontaine, T., et al. (2011). "Galactosaminogalactan, a New Immunosuppressive Polysaccharide of Aspergillus fumigatus." PloS pathog. **7**(11).

65 Ouyang, H., et al. (2013). "One single basic amino acid at ω-1 or ω-2 site is a signal that retains glycosylphosphatidylinositol (GPI) anchored protein in plasma membrane of Aspergillus fumigatus." Eukaryot. Cell **12**(6): 889-899.

66 McDermott, A. (2009). "Structure and Dynamics of Membrane Proteins by Magic Angle Spinning Solid-State NMR." Annu. Rev. Biophys. **38**: 385-403.

67 Marchanka, A., et al. (2015). "RNA structure determination by solid-state NMR spectroscopy." Nat. Commun. **6**: 7024.

68 Meier, B. H., et al. (2017). "Emerging Structural Understanding of Amyloid Fibrils by Solid-State NMR." Trends Biochem. Sci. **42**(10): 777-787.

69 Comellas, G. and C. M. Rienstra (2013). "Protein Structure Determination by Magic-Angle Spinning Solid-State NMR, and Insights into the Formation, Structure, and Stability of Amyloid Fibrils." Annu. Rev. Biophys. **42**: 515-536.

70 Mandala, V. S., et al. (2018). "Structure and Dynamics of Membrane Proteins from Solid-State NMR." Annu. Rev. Biophys. **47**: 201-222.

71 Quinn, C. M. and T. Polenova (2017). "Structural biology of supramolecular assemblies by magic-angle spinning NMR spectroscopy." Q. Rev. Biophys. **50**.

72 Kang, X., et al. (2019). "Lignin-polysaccharide interactions in plant secondary cell walls revealed by solid-state NMR." Nat. Commun. **10**(1): 347.

73 Wang, T., et al. (2013). "Sensitivity-enhanced solid-state NMR detection of expansin's target in plant cell walls." Proc. Natl. Acad. Sci. USA **110**(41): 16444-16449.

74 Frederick, K. K., et al. (2015). "Sensitivity-Enhanced NMR Reveals Alterations in Protein Structure by Cellular Milieus." Cell **163**(3): 620-628.

75 Albert, B. J., et al. (2018). "Dynamic Nuclear Polarization Nuclear Magnetic Resonance in Human Cells Using Fluorescent Polarizing Agents." Biochemistry **57**(31): 4741-4746.

76 Sergeyev, I. V., et al. (2017). "Efficient assignment and NMR analysis of an intact virus using sequential side-chain correlations and DNP sensitization." Proc. Natl. Acad. Sci. USA **114**(20): 5171-5176.

77 Mentink-Vigier, F., et al. (2015). "Theoretical aspects of Magic Angle Spinning - Dynamic Nuclear Polarization." J. Magn. Reson. **258**: 102-120.

78 Ni, Q. Z., et al. (2013). "High Frequency Dynamic Nuclear Polarization." Acc. Chem. Res. **46**: 1933-1941.

79 Rossini, A. J., et al. (2013). "Dynamic Nuclear Polarization Surface Enhanced NMR Spectroscopy." Acc. Chem. Res. **46**(9): 1942-1951.

80 Liao, S. Y., et al. (2016). "Efficient DNP NMR of membrane proteins: sample preparation protocols, sensitivity, and radical location." J. Biomol. NMR **64**(3): 223-237.

81 Kirui, A., et al. (2019). "Preparation of Fungal and Plant Materials for Structural Elucidation Using Dynamic Nuclear Polarization Solid-State NMR." J. Vis. Exp. **144**: e59152.

82 Song, C. S., et al. (2006). "TOTAPOL: A biradical polarizing agent for dynamic nuclear polarization experiments in aqueous media." J. Am. Chem. Soc. **128**(35): 11385-11390.

83 Sauvee, C., et al. (2013). "Highly Efficient, Water-Soluble Polarizing Agents for Dynamic Nuclear Polarization at High Frequency." Angew. Chem. Int. Edit. **52**(41): 10858-10861.

84 Mentink-Vigier, F., et al. (2018). "Computationally Assisted Design of Polarizing Agents for Dynamic Nuclear Polarization Enhanced NMR: The AsymPol Family." J. Am. Chem. Soc. **140**(35): 11013-11019.

85 Smith, A. N., et al. (2015). "A method for dynamic nuclear polarization enhancement of membrane proteins." Angew. Chem. Int. Ed. Engl. **54**(5): 1542-1546.

86 Marin-Montesinos, I., et al. (2019). "Selective high-resolution DNP-enhanced NMR of biomolecular binding sites." Chem. Sci. **10**(11): 3366-3374.

87 Joh, N. H., et al. (2014). "De novo design of a transmembrane Zn^{2+}-transporting four-helix bundle." Science **346**(6216): 1520-1524.

88 Williamson, M. P. (2013). "Using chemical shift perturbation to characterise ligand binding." Prog. Nucl. Mag. Res. Sp. **73**: 1-16.

89 Charlton, A. J., et al. (2002). "Polyphenol/peptide binding and precipitation." J. Agr. Food Chem. **50**(6): 1593-1601.

90 Schmidt, N. W., et al. (2013). "Influenza Virus A M2 Protein Generates Negative Gaussian Membrane Curvature Necessary for Budding and Scission." J. Am. Chem. Soc. **135**(37): 13710-13719.

91 Wang, T., et al. (2012). "NMR Determination of Protein Partitioning into Membrane Domains with Different Curvatures and Application to the Influenza M2 Peptide." Biophys. J. **102**(4): 787-794.

92 Wang, T. and M. Hong (2015). "Investigation of the curvature induction and membrane localization of the influenza virus M2 protein using static and off-magic-angle spinning solid-state nuclear magnetic resonance of oriented bicelles." Biochemistry **54**(13): 2214-2226.

93 Rossman, J. S., et al. (2010). "Influenza Virus M2 Protein Mediates ESCRT-Independent Membrane Scission." Cell **142**(6): 902-913.

94 van der Cruijsen, E. A. W., et al. (2015). "Biomolecular DNP-Supported NMR Spectroscopy using Site-Directed Spin Labeling." Chem. Eur. J. **21**(37): 12971-12977.

95 Wylie, B. J., et al. (2015). "Dynamic nuclear polarization of membrane proteins: covalently bound spin-labels at protein-protein interfaces." J. Biomol. NMR **61**(3-4): 361-367.

96 Voinov, M. A., et al. (2015). "Cysteine-Specific Labeling of Proteins with a Nitroxide Biradical for Dynamic Nuclear Polarization NMR." J. Phys. Chem. B **119**(32): 10180-10190.

97 Rogawski, R., et al. (2017). "NMR Signal Quenching from Bound Biradical Affinity Reagents in DNP Samples." J. Phys. Chem. B **121**(48): 10770-10781.

98 Wang, T., et al. (2015). "Relaxation-compensated difference spin diffusion NMR for detecting 13C-13C long-range correlations in proteins and polysaccharides." J. Biomol. NMR **61**(2): 97-107.

99 Wang, T., et al. (2016). "The Target of beta-Expansin EXPB1 in Maize Cell Walls from Binding and Solid-State NMR Studies." Plant Physiol. **172**(4): 2107-2119.

100 Kaplan, M., et al. (2015). "Probing a cell-embedded megadalton protein complex by DNP-supported solid-state NMR." Nat. Methods **12**(7): 649-+.

101 Frederick, K. K., et al. (2017). "Combining DNP NMR with segmental and specific labeling to study a yeast prion protein strain that is not parallel in-register." Proc. Natl. Acad. Sci. USA **114**(14): 3642-3647.

102 Narasimhan, S., et al. (2019). "DNP-Supported Solid-State NMR Spectroscopy of Proteins Inside Mammalian Cells." Angew. Chem. Int. Edit. **58**(37): 12969-12973.

103 McCoy, K. M., et al. (2019). "Stability of nitroxide biradical TOTAPOL in biological samples." J. Magn. Reson. **303**: 115-120.

104 Schlagnitweit, J., et al. (2019). "Observing an Antisense Drug Complex in Intact Human Cells by in-Cell NMR Spectroscopy." ChemBioChem **20**(19): 2474-2478.

105 Cosgrove, D. J. (2001). "Wall structure and wall loosening. A look backwards and forwards." Plant Physiol. **125**(1): 131-134.

106 Wang, T., et al. (2016). "Multidimensional solid-state NMR spectroscopy of plant cell walls." Solid State Nucl. Magn. Reson. **78**: 56-63.

107 Nygaard, R., et al. (2015). "Spectral snapshots of bacterial cell-wall composition and the influence of antibiotics by whole-cell NMR." Biophys. J. **108**(6): 1380-1389.

108 Arnold, A. A., et al. (2018). "Whole cell solid-state NMR study of Chlamydomonas reinhardtii microalgae." J. Biomol. NMR **70**(2): 123-131.

109 Chatterjee, S., et al. (2015). "Solid-state NMR Reveals the Carbon-based Molecular Architecture of Cryptococcus neoformans Fungal Eumelanins in the Cell Wall." J. Biol. Chem. **290**(22): 13779-13790.

110 Chatterjee, S., et al. (2018). "The melanization road more traveled by: Precursor substrate effects on melanin synthesis in cell-free and fungal cell systems." J. Biol. Chem. **293**(52): 20157-20168.

111 Terrett, O. M., et al. (2019). "Molecular architecture of softwood revealed by solid-state NMR." Nat. Commun. **10**(1): 4978.

112 Simmons, T. J., et al. (2016). "Folding of xylan onto cellulose fibrils in plant cell walls revealed by solid-state NMR." Nat. Commun. **7**: 13902.

113 Kirui, A., et al. (2019). "Atomic Resolution of Cotton Cellulose Structure Enabled by Dynamic Nuclear Polarization Solid-State NMR." Cellulose **26**: 329-339.

114 Kono, H. (2004). "Two-dimensional magic angle spinning NMR investigation of naturally occurring chitins: Precise H-1 and C-13 resonance assignment of alpha- and beta-chitin." Biopolymers **75**(3): 255-263.

115 Kameda, T., et al. (2004). "Hydrogen bonding structure and stability of alpha-chitin studied by C-13 solid-state NMR." Macromol. Biosci. **5**(2): 103-106.

116 Sikorski, P., et al. (2009). "Revisit of alpha-Chitin Crystal Structure Using High Resolution X-ray Diffraction Data." Biomacromolecules **10**(5): 1100-1105.

117 Yui, T., et al. (2007). "Exhaustive crystal structure search and crystal modeling of beta-chitin." Int. J. Biol. Macromol. **40**(4): 336-344.

118 Lewandowski, J. R., et al. (2009). "^{15}N-^{15}N proton assisted recoupling in magic angle spinning NMR." J. Am. Chem. Soc. **131**(16): 5769-5776.

119 De Paepe, G., et al. (2008). "Proton assisted recoupling and protein structure determination." J. Chem. Phys. **129**(24).

120 Donovan, K. J., et al. (2017). "Proton-Assisted Recoupling (PAR) in Peptides and Proteins." J. Phys. Chem. B **121**(48): 10804-10817.

121 Dubroca, T., et al. (2018). "A quasi-optical and corrugated waveguide microwave transmission system for simultaneous dynamic nuclear polarization NMR on two separate 14.1 T spectrometers." J. Magn. Reson. **289**: 35-44.

122 Viger-Gravel, J., et al. (2019). "Topology of Pretreated Wood Fibers Using Dynamic Nuclear Polarization." J. Phys. Chem. C. **123**(50): 30407-30415.

123 Perras, F. A., et al. (2017). "Atomic-Level Structure Characterization of Biomass Pre- and Post-Lignin Treatment by Dynamic Nuclear Polarization-Enhanced Solid-State NMR." J. Phys. Chem. A **121**(3): 623-630.

124 Quinn, C. M., et al. (2018). "Dynamic regulation of HIV-1 capsid interaction with the restriction factor TRIM5 alpha identified by magic-angle spinning NMR and molecular dynamics simulations." Proc. Natl. Acad. Sci. USA **115**(45): 11519-11524.

125 Gupta, R., et al. (2016). "Dynamic Nuclear Polarization Enhanced MAS NMR Spectroscopy for Structural Analysis of HIV-1 Protein Assemblies." J. Phys. Chem. B. **120**(2): 329-339.

126 Takahashi, H., et al. (2013). "Solid-state NMR on bacterial cells: selective cell wall signal enhancement and resolution improvement using dynamic nuclear polarization." J. Am. Chem. Soc. **135**(13): 5105-5110.

127 Azais, T., et al. (2019). "Structural description of surfaces and interfaces in biominerals by DNP SENS." Solid State Nucl. Magn. Reson. **102**: 2-11.

128 Goldberga, I., et al. (2019). "Detection of nucleic acids and other low abundance components in native bone and osteosarcoma extracellular matrix by isotope enrichment and DNP-enhanced NMR." RSC Adv. **9**(46): 26686-26690.

129 Chow, W. Y., et al. (2018). "Essential but sparse collagen hydroxylysyl post-translational modifications detected by DNP NMR." Chem. Commun. **54**(89): 12570-12573.

130 Lu, M. M., et al. (2019). "^{19}F Dynamic Nuclear Polarization at Fast Magic Angle Spinning for NMR of HIV-1 Capsid Protein Assemblies." J. Am. Chem. Soc. **141**(14): 5681-5691.

131 Smith, A. N., et al. (2019). "Natural Isotopic Abundance ^{13}C and ^{15}N Multidimensional Solid-State NMR Enabled by Dynamic Nuclear Polarization." J. Phys. Chem. Lett. **10**(16): 4652-4662.

132 Smith, A. N., et al. (2018). "Structural Fingerprinting of Protein Aggregates by Dynamic Nuclear Polarization-Enhanced Solid-State NMR at Natural Isotopic Abundance." J. Am. Chem. Soc. **140**(44): 14576-14580.

133 Marker, K., et al. (2017). "Welcoming natural isotopic abundance in solid-state NMR: probing pi-stacking and supramolecular structure of organic nanoassemblies using DNP." Chem. Sci. **8**(2): 974-987.

134 Ling, Z., et al. (2019). "Effects of ball milling on the structure of cotton cellulose." Cellulose **26**(1): 305-328.

135 Shim, J. H., et al. (2007). "Antitumor effect of soluble beta-1,3-glucan from Agrobacterium sp. R259 KCTC 1019." J. Microbiol. Biotechnol. **17**(9): 1513-1520.

136 Fairweather, J. K., et al. (2009). "Structural characterization by 13C-NMR spectroscopy of products synthesized in vitro by polysaccharide synthases using 13C-enriched glycosyl donors: application to a UDP-glucose:(1→3)- β -d-glucan synthase from blackberry (Rubus fruticosus) " Glycobiology **14**(9): 775-781.

137 Saitô, H., et al. (1979). "A 13C-nuclear magnetic resonance study of polysaccharide gels. Molecular architecture in the gels consisting of fungal, branched (1 → 3)- β -d-glucans (lentinan and schizophyllan) as manifested by conformational changes induced by sodium hydroxide." Carbohydr. Res. **74**(1): 227-240.

138 Bhanja, S. K., et al. (2014). "Water-insoluble glucans from the edible fungus Ramaria botrytis." Bioactive Carbohydrates and Dietary Fibre **3**(2): 52-58.

139 Puanglek, S., et al. (2016). "In vitro synthesis of linear alpha-1,3-glucan and chemical modification to ester derivatives exhibiting outstanding thermal properties." Sci. Rep. **6**.

140 Kono, H., et al. (2004). "^{13}C and ^{1}H resonance assignment of mercerized cellulose II by two-dimensional MAS NMR spectroscopies." Macromolecules **37**(14): 5310-5316.

141 Heux, L., et al. (2000). "Solid state NMR for determination of degree of acetylation of chitin and chitosan." Biomacromolecules **1**(4): 746-751.

142 King, C., et al. (2017). "Measuring the Purity of Chitin with a Clean, Quantitative Solid-State NMR Method." ACS Sustain. Chem. Eng. **5**(9): 8011-8016.

143 Tanner, S. F., et al. (1990). "High-Resolution Solid-State C-13 Nuclear-Magnetic-Resonance Study of Chitin." Macromolecules **23**(15): 3576-3583.

144 Fritzsching, K. J., et al. (2013). "Practical use of chemical shift databases for protein solid-state NMR: 2D chemical shift maps and amino-acid assignment with secondary-structure information." J Biomol NMR **56**(2): 155-167.

Vita

Arnab Chakraborty was born and raised in Dhaka, Bangladesh and his ancestors were from Barisal, Shikerpur, Wazirpur. He earned his bachelor's degree in chemistry from the University of Dhaka on May 2017. Arnab joined Louisiana State University in the Fall of 2018, where he focused on characterization of the polysaccharides and proteins present in *Aspergillus fumigatus* cell wall. His work has resulted in two publications as first author. He will start his career in PPD at Madison, Wisconsin as an Associate Scientist. He plans to graduate in August 2022.